

1 **Dust storms from the Taklamakan Desert significantly darken snow**
2 **surface on surrounding mountains**

3 Yuxuan Xing¹, Yang Chen¹, Shirui Yan¹, Tenglong Shi^{1,2}, Xiaoyi Cao¹, Xiaoying Niu¹,
4 Dongyou Wu¹, Jiecan Cui^{1,3,2}, Xin Wang^{1,3}, Yue Zhou¹, Wei Pu¹

5 ¹Key Laboratory for Semi-Arid Climate Change of the Ministry of Education, College of Atmospheric
6 Sciences, Lanzhou University, Lanzhou 730000, China

7 ² Henan Industrial Technology Academy of Spatial-Temporal Big Data, Henan University, Kaifeng
8 475004, China

9 ~~Zhejiang Development & Planning Institute, Hangzhou 310030, China~~

10 ³Zhejiang Development & Planning Institute, Hangzhou 310030, China

11 ~~Institute of Surface Earth System Science, Tianjin University, Tianjin 300072, China~~

12 *Correspondence to:* Wei Pu (puwei@lzu.edu.cn)

13

14 **Abstract**

15 The Taklamakan Desert (TD) is a major source of mineral dust emissions into the
16 atmosphere. These dust particles have the ability to darken the surface of snow on the
17 surrounding high mountains after deposition, significantly impacting the regional
18 radiation balance. However, previous field measurements have been unable to capture
19 the effects of severe dust storms accurately, and their representation on regional scales
20 has been inadequate. In this study, we propose a modified remote-sensing approach that
21 combines data from the Moderate Resolution Imaging Spectroradiometer (MODIS)
22 satellite and simulations from the Snow, Ice, and Aerosol Radiative (SNICAR) model.
23 This approach allows us to detect and analyze the substantial snow darkening resulting
24 from dust storm deposition. We focus on three typical dust events originating from the
25 Taklamakan Desert and observe significant snow darkening over an area of ~2160,
26 ~610, and ~640~~>2100, >600, and >630~~ km² in the Tien Shan, Kunlun, and Qilian
27 Mountains, respectively. Our findings reveal that the impact of dust storms extends
28 beyond the local high mountains, reaching mountains located approximately 1000 km
29 away from the source. Furthermore, we observe that dust storms not only darken the
30 snowpack during the spring but also in the summer and autumn seasons, leading to
31 increased absorption of solar radiation. Specifically, the snow albedo reduction
32 (radiative forcing) triggered by severe dust depositions is up to 0.028–0.079 (11–31.5
33 W m⁻²), 0.088–0.136 (31–49 W m⁻²), and 0.092–0.153 (22–38 W m⁻²) across the Tien
34 Shan, Kunlun, and Qilian Mountains, respectively. This further contributes to the aging
35 of the snow, as evidenced by the growth of snow grain size. Comparatively, the impact
36 of persistent but relatively slow dust deposition over several months during non-event
37 periods is significantly lower than that of individual dust event. This highlights the
38 necessity of giving more attention to the influence of extreme events on the regional
39 radiation balance. ~~From~~Through this study, we gain a deeper understanding of how a
40 single dust event can affect the extensive snowpack and demonstrates the potential of
41 employing satellite remote-sensing to monitor large-scale snow darkening.

42 **1 Introduction**

43 High Mountain Asia (HMA), which includes the Tibetan Plateau (TP) and surrounding
44 mountain ranges, holds the largest amount of glaciers and snow outside of the poles.
45 This region is informally known as the “The Third Pole” and the “Asian Water Tower”
46 (Yao et al., 2012, 2019) because of its extreme importance as a freshwater source, with
47 approximately one billion people relying on the water and hydropower that the glaciers
48 and snow across HMA regularly provide (Immerzeel et al., 2012; Mishra et al., 2018).
49 The snow-covered area of HMA is a highly reflective natural surface that has a
50 significant impact on the regional radiation balance (Cohen and Rind, 1991; Painter et
51 al., 2012). Previous satellite- and ground-based observations have demonstrated that
52 the mass and extent of the snow cover across HMA are rapidly declining owing to
53 recent global warming (Bormann et al., 2018; Notarnicola et al., 2020; Pulliainen et al.,
54 2020). Furthermore, growing evidence has indicated that light-absorbing particles
55 (LAPs) ([Arun et al., 2019, 2021a, 2021b](#); [Chaubey et al., 2010](#); [Gogoi et al., 2018,](#)
56 [2021a; 2021b](#); [Thakur et al., 2021](#)), such as mineral dust and black carbon (BC), can
57 induce snow darkening effect when they are deposited on the snow surface (Wang et
58 al., 2013; Qian et al., 2015; Dang et al., 2017; Huang et al., 2022; Niu et al., 2022;
59 Réveillet et al., 2022). This snow darkening effect increases solar absorption and
60 decreases snow albedo, resulting in enhanced snowmelt ~~and an imbalance in the Asian~~
61 ~~Water Tower~~ (Hadley and Kirchstetter, 2012; Dumont et al., 2014; He et al., 2017, 2018;
62 Shi et al., 2021, 2022a, 2022b; Cordero et al., 2022) ~~and an accelerated transformation~~
63 ~~of ice and snow into liquid water in the Asian Water Tower~~ (Yao et al., 2022).
64 Consequently, the snow-darkening effect plays a critical role in snow decline across
65 HMA, thereby perturbing the climate system and impacting hydrological cycles
66 (Kraaijenbrink et al., 2017, 2021; Sang et al., 2019; Shi et al., 2019; Zhang et al., 2020,
67 2021; Roychoudhury et al., 2022; Yang et al., 2022).

68 The Taklamakan Desert (TD) in southwestern Xinjiang, Northwest China, is the
69 second-largest shifting sand desert on Earth and accounts for 42% of all dust emissions
70 in East Asia (Chen et al., 2017a). Approximately 70.54 Tg of dust are emitted into the
71 atmosphere annually, with the most intense dust events occurring in spring (Chen et al.,
72 2017a). The dust in the Tarim Basin is predominantly redeposited onto nearby regions

73 owing to the surrounding high mountains (Qiu et al., 2001; Sun et al., 2001; Shao and
74 Dong, 2006). When the dust is uplifted above 4 km altitude, it may eventually settle on
75 the snow surfaces across the surrounding high mountains, such as the Tien Shan and
76 Kunlun Mountains and subsequently induce a snow-darkening effect (Ge et al., 2014;
77 Jia et al., 2015; Yuan et al., 2018). Furthermore, this dust is also transported eastward
78 beyond the Tarim Basin and can be transported all the way to the Qilian Mountains via
79 the westerly winds during spring and summer, thereby inducing a snow darkening effect
80 in this distal region to the east of the TD (Dong et al., 2020; Han et al., 2022). Therefore,
81 TD dust may have a profound effect on the regional radiative balance by darkening the
82 snow across the high mountains surrounding the TD. This effect may subsequently
83 accelerate snow melting and affect water resources for the 30+ million people living in
84 the Xinjiang and Gansu provinces of China (Mishra et al., 2021).

85 Numerous field measurements have been undertaken in recent decades to investigate
86 the dust content of snow/glaciers across the high mountains surrounding the TD, with
87 measured dust contents generally varying from 1.4 to 110 $\mu\text{g g}^{-1}$ (Wake et al., 1994;
88 Dong et al., 2009, 2014; Wu et al., 2010; Ming et al., 2016; Xu et al., 2016; Schmale et
89 al., 2017; Zhang et al., 2018, 2021; Wang et al., 2019; Li et al., 2021, 2022). This
90 abundance of dust particles has been found to induce a significant snow darkening
91 effect across the high-mountain snowpack, thereby increasing its associated radiative
92 forcing to 25.8–65.7 W m^{-2} . Furthermore, the estimated natural dust-induced snow-
93 darkening effect can be equivalent to that induced by BC, particularly during intense
94 springtime dust events —(Sarangi et al., 2020; Zhang et al., 2021). These findings
95 effectively highlight the significance of the TD dust-induced snow darkening effect
96 across the surrounding high mountains. In spite of these invaluable in situ findings,
97 ground-based observations are poorly represented at the regional scale owing to limited
98 spatial coverage and temporal discontinuity (Arun et al., 2019). Furthermore, these
99 previous field measurements may not be able to capture severe dust emission and
100 loading events, which are more likely to induce snow darkening than common dry and
101 wet deposition processes (Dumont et al., 2020; Pu et al., 2021; Baladima et al., 2022).

102 Satellite remote sensing offers an effective way to overcome the limitations of ground-
103 based measurements by providing a more comprehensive understanding of the LAP-
104 induced impact on the regional radiative forcing of the snowpack (Skiles et al., 2018a).
105 For example, Painter et al. (2012) found that the instantaneous LAP-induced radiative
106 forcing can exceed 250 W m^{-2} in the Hindu Kush-Himalaya region via an analysis of
107 Moderate Resolution Imaging Spectroradiometer (MODIS) satellite data. Sarangi et al.
108 (2020) further revealed that dust is the primary factor responsible for high-altitude snow
109 darkening in the Hindu Kush–Himalaya region. Similarly, severe dust events from the
110 Sahara can deposit dust on the snowpack across the European Alps and Caucasus
111 Mountains (Di Mauro et al., 2015; Dumont et al., 2020), with this deposition inducing
112 a radiative forcing of up to 153 W m^{-2} based on satellite retrievals in Europe. Dust
113 deposition has also induced extensive snow darkening across the Upper Colorado River
114 Basin in North America, particularly during extreme dust events (Skiles et al., 2016,
115 2018b; Painter et al., 2017). These studies have demonstrated the effectiveness of
116 employing satellite remote sensing to estimate the dust content of the snowpack and its
117 associated radiative forcing. However, detecting natural dust deposition on the snow
118 surfaces across high mountains surrounding the TD is still limited.

119 Here we investigate the impact of dust storms on snow albedo reduction and radiative
120 forcing across the high mountains surrounding the TD. We first capture three typical
121 dust events that induced snow darkening in the Tien Shan, Kunlun, and Qilian
122 Mountains, respectively. We ~~then first~~ utilize MODIS satellite data and the Snow, Ice,
123 and Aerosol Radiative (SNICAR) model to retrieve the dust content of the snowpack.
124 We then capture three typical dust events that induced snow darkening in the Tien Shan,
125 Kunlun, and Qilian Mountains, respectively. Finally, we analyze the spatial and
126 altitudinal variations in dust-induced snow darkening and compare our retrievals with
127 field measurements. Through remote sensing observations, we aim to provide a new
128 view of the darkening effect of natural desert dust on the snowpack of the high
129 mountains surrounding the TD.

130 **2 Methodology**

131 2.1 Remote-sensing data

132 We accessed two MODIS datasets, the surface reflectance (MOD09GA:
133 <https://earthdata.nasa.gov>; 500 × 500 m resolution) and aerosol optical depth (AOD;
134 MCD19A2), to evaluate the impact of dust on snow albedo. MOD09GA is the daily
135 surface reflectance product after the atmospheric correction from the Terra satellite,
136 which provides the reflectance data for seven bands (band 1, 620–670 nm; band 2, 841–
137 876 nm; band 3, 459–479 nm; band 4, 545–565 nm; band 5, 1230–1250 nm; band 6,
138 1628–1652 nm; band 7, 2105–2155 nm). Previous studies have indicated that the
139 MODIS sensor on Terra is not affected by saturation on bright snow surfaces. As a result,
140 it has the capability of detecting changes in reflectance in the visible (VIS) bands caused
141 by dust in snow (Painter et al., 2012; Pu et al., 2019). Additionally, we used the updated
142 MODIS Aerosol Optical Depth (AOD) product MCD19A2, based on the MAIAC
143 algorithm, to assess the AOD levels during dust events. This is a combined product of
144 Terra/Aqua with a spatial-temporal resolution of 1km, which were resampled to 500m
145 resolution using GEE (<https://earthengine.google.com>).

146 The daily averaged downward shortwave flux was obtained from the NASA Clouds
147 and the Earth's Radiant Energy System (CERES: <https://ceres.larc.nasa.gov>; 1° × 1°
148 resolution). The CERES data products take advantage of the synergy between
149 collocated CERES instruments and spectral imagers, such as MODIS (Terra and Aqua)
150 and the Visual Infrared Imaging Radiometer Suite (S-NPP and NOAA-20). We used the
151 downward shortwave flux to estimate the daily averaged radiative forcing that was due
152 to dust deposition on the snowpack. The Cloud-Aerosol Lidar with Orthogonal
153 Polarization (CALIOP/CALIPSO) provided by NASA is able to detect the type and
154 height of aerosols in the atmosphere (Huang et al., 2007; Han et al., 2022) and can
155 therefore be used to identify the movement of dust storms over the high mountains
156 surrounding the TD.

157 The Shuttle Radar Topography Mission (SRTM) digital elevation data, which possess
158 a 90-m spatial resolution, were provided by NASA and downloaded from Google Earth
159 Engine (<https://earthengine.google.com>). These data were used to correct the influence
160 of topography on surface reflectance.

161 **2.2 Snow depth and wind data**

162 The snow depth data were provided by NASA and accessed from the Modern-Era
163 Retrospective Analysis for Research and Applications, Version 2 (MERRA-2:
164 <https://gmao.gsfc.nasa.gov>). The MERRA-2 snow depth product was selected because
165 it has better accuracy than those from ERA-Interim, JJA-55, and ERA5 across HMA
166 (Orsolini et al, 2019). The wind field data were obtained from the European Centre for
167 Medium-Range Weather Forecasts (ECMWF) Reanalysis v5 (ERA5:
168 <https://www.ecmwf.int>) owing to its superior performance in terms of its high spatial
169 resolution and longer time span compared with other products (Copernicus Climate
170 Change Service, 2017). Here, we used ERA5 wind data at 700 hPa to describe the
171 atmospheric circulation during the analyzed dust storms.

172 **2.3 Radiative-transfer model**

173 The SNICAR model is a two-stream radiative transfer model (Flanner et al., 2007, 2009)
174 that has been widely used to simulate the spectral albedo of LAP-contaminated snow
175 (Sarangi et al., 2019; Chen et al., 2021). The model includes snow properties such as
176 snow depth and effective radius and accounts for the incident radiation at the surface
177 and its spectral distribution, solar zenith angle, and the type and concentration of LAPs
178 in the snowpack. In this study, dust optical parameters are taken from SNICAR defaults,
179 where the refractive index is $1.56 + 0.0038i$ at $0.63 \mu\text{m}$ (Patterson et al., 1981; [Flanner
180 et al., 2007](#)). And a diameter bin of $0.1\text{-}1 \mu\text{m}$ was selected according to the previous
181 observations from Taklamakan Desert (Okada and Kai, 2004). [Furthermore, a single-
182 layer snowpack model was adopted in our study, in line with Cui et al. \(2021\), since the
183 snow darkening effect typically pertains to surface snow. This simplification minimally
184 affects the retrieval of LAPs from the surface snow, despite the complex multilayer
185 structure of natural snowpacks.](#)

186 The Santa Barbara DISORT Atmospheric Radiative Transfer (SBDART) model is one
187 of the most widely used models for simulating the surface solar irradiance in clear and
188 cloudy sky conditions (Ricchiazzi et al., 1998). The SBDART model includes standard
189 atmospheric models, cloud models, extraterrestrial source spectra, gas absorption
190 models, standard aerosol models, and surface models. Here, we used the SBDART

191 model to calculate the spectral surface solar irradiance, following the approach of Cui
192 et al. (2021). In this study, the cloud-free condition was set in SBDART, according to
193 the MODIS images.

194 **2.4 Terrain correction**

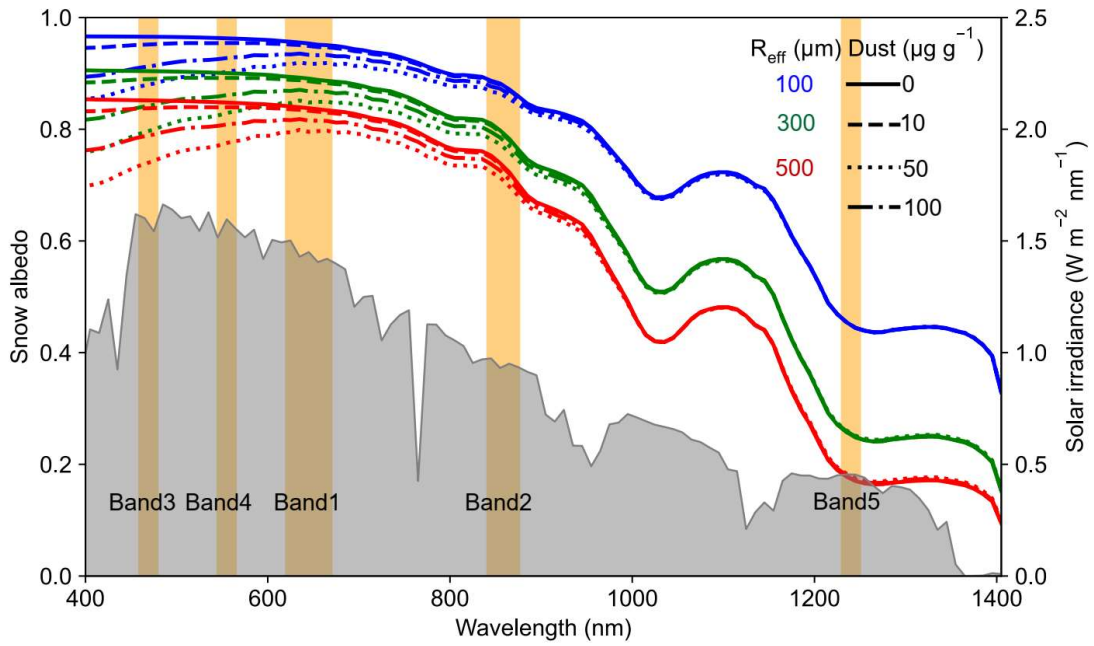
195 The high mountains surrounding the TD have a complex terrain, such that the local
196 solar zenith angle (β) may differ from the MODIS-derived solar zenith angle (θ_0).
197 Therefore, the topographic correction method should be used to derive β (Teillet et al.,
198 1982; Negi and Kokhanovsky, 2011):

$$199 \cos \beta = \cos \theta_0 \cos \theta_T + \sin \theta_0 \sin \theta_T \cos (\phi_0 - \phi_T), \quad (1)$$

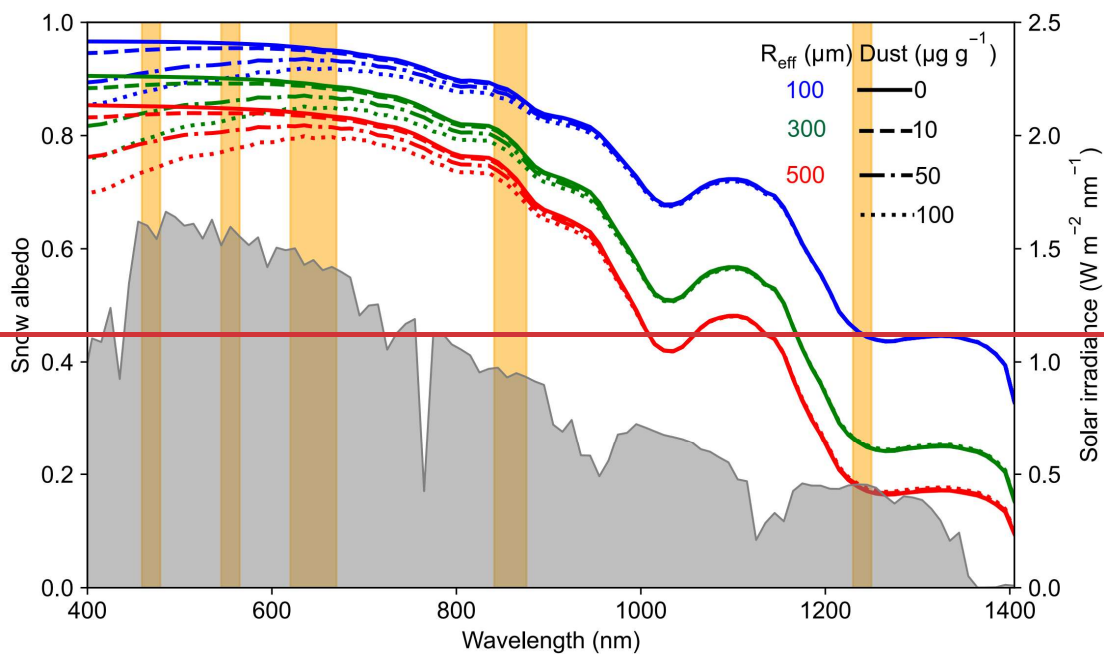
200 where ϕ_0 is the solar azimuth angle from MODIS, and θ_T and ϕ_T are the surface
201 slope and aspect from SRTM, respectively. We then replace θ_0 with β in subsequent
202 satellite retrievals.

203 **2.5 Snow properties retrieval**

204 The dust-contaminated spectral snow albedo is determined based on the dust content,
205 snow grain size, snow depth, and solar zenith angle (Wiscombe and Warren, 1980). The
206 dust content and snow depth primarily impact the snow albedo in the ultraviolet (UV)
207 and VIS wavelengths, with a much smaller effect on snow albedo in the near infrared
208 (NIR) wavelengths (Figure 1 and Figure S1). Conversely, the snow grain size and solar
209 zenith angle primarily impact the snow albedo in the NIR wavelengths. The solar zenith
210 angle and snow depth data are from MODIS Terra and MERRA-2, respectively. We
211 used the SNICAR model to derive the quantitative snow grain size and dust content
212 from the MODIS data. ~~We then used~~ the SBDART model was combined to estimate
213 the dust-induced snow albedo reduction and radiative forcing. Figure 2 shows the
214 flowchart of the overall retrieval process.



215



216

217 **Figure 1. Snow albedo spectra for different snow optical effective radius (R_{eff}) and**
 218 **dust contents that were simulated using the SNICAR model. Orange bars denote**
 219 **MODIS bands, and the gray region represents the typical solar irradiance in HMA.**

220 The Snow-Covered Area and Grain size (SCAG) model is a spectral unmixing method
 221 that is widely used for identifying snow cover fraction (SCF) and snow optical effective
 222 radius (R_{eff}), especially in complex mountain terrains (Painter et al., 2009, 2012; Rittger
 223 et al., 2013). The SCAG model retrieves the SCF and R_{eff} using all seven bands of the

224 MODIS reflectance data, which span the VIS to NIR range. It does not consider the
 225 impact of LAPs. However, in our study, the dust content in snow is extreme high, which
 226 will significantly reduce the VIS snow albedo in MODIS bands 1, 3, 4 (Figure 1). So,
 227 the SCAG model will introduce a large bias in the resultant SCF and R_{eff} retrievals.
 228 Furthermore, the reflectance of fine-grained dirty snow has been compared with that of
 229 pure coarse-grained snow at short-wave infrared wavelengths, which include bands 6
 230 and 7 (Bair et al., 2020). The extremely high dust content in this study therefore means
 231 that the reflectance in MODIS bands 6 and 7 is not appropriate for snow property
 232 retrieval. Instead, we used the reflectance data in MODIS bands 2 and 5 to unmix the
 233 surface reflectance to derive SCF and R_{eff} (Figure 2), similar to the approach in Painter
 234 et al. (2009). The surface reflectance at band i ($R_{\text{band } i}^{\text{MODIS}}$) can be expressed as follows
 235 (Cui et al., 2021):

$$236 \quad R_{\text{band } i}^{\text{MODIS}} = \frac{E_{\text{band } i} \times \text{SCF} \times R_{\text{band } i}^{\text{MODIS, snow}} + E_{\text{band } i} \times (1 - \text{SCF}) \times R_{\text{band } i}^{\text{soil}}}{E_{\text{band } i}}$$

$$237 \quad = \text{SCF} \times R_{\text{band } i}^{\text{MODIS, snow}} + (1 - \text{SCF}) \times R_{\text{band } i}^{\text{soil}}, \quad (2)$$

238 where $R_{\text{band } i}^{\text{MODIS, snow}}$ and $R_{\text{band } i}^{\text{soil}}$ represent the snow and soil reflectances at band i ,
 239 respectively, with $R_{\text{band } i}^{\text{soil}}$ taken from Siegmund and Menz (2005), and $E_{\text{band } i}$ is the
 240 solar irradiance at band i . The snow reflectance at band i ($R_{\text{band } i}^{\text{MODIS, snow}}$) can be
 241 expressed as

$$242 \quad R_{\text{band } i}^{\text{MODIS, snow}} = \left(\frac{R_{\text{band } i}^{\text{MODIS}} - (1 - \text{SCF}) \times R_{\text{band } i}^{\text{soil}}}{\text{SCF}} \right). \quad (3)$$

243 We then fit the SNICAR-simulated snow reflectance to the MODIS-derived snow
 244 reflectance, which is expressed as either

$$245 \quad \text{RMSE} = \left(\frac{1}{2} (a \times (R_{\text{band } 2}^{\text{SNICAR, snow}} - R_{\text{band } 2}^{\text{MODIS, snow}})^2 + (R_{\text{band } 5}^{\text{SNICAR, snow}} - R_{\text{band } 5}^{\text{MODIS, snow}})^2) \right)^{\frac{1}{2}} \quad (4)$$

246 or

$$247 \quad \text{RMSE} = \left(\frac{1}{2} (a \times (R_{\text{band } 2}^{\text{SNICAR, snow}} - \left(\frac{R_{\text{band } 2}^{\text{MODIS}} - (1 - \text{SCF}) \times R_{\text{band } 2}^{\text{soil}}}{\text{SCF}} \right))^2 \right)$$

248
$$+(R_{\text{band } 5}^{\text{SNICAR, snow}} - \left(\frac{R_{\text{band } 5}^{\text{MODIS}} - (1 - \text{SCF}) \times R_{\text{band } 5}^{\text{soil}}}{\text{SCF}} \right)^2)^{\frac{1}{2}}, \quad (5)$$

249 where RMSE is the root mean square error, $R_{\text{band } i}^{\text{SNICAR, snow}}$ is the SNICAR-simulated
 250 snow reflectance at band i (which is dependent on the R_{eff} and solar zenith angle, where
 251 the solar zenith angle is derived from the MODIS data), and a is an empirical coefficient
 252 (0.1–1 range). In this study, a was set to 0.1 to reduce the interference of dust on the
 253 snow properties retrieval because a high dust content can influence the snow albedo at
 254 band 2 (Figure 1). We can then derive SCF and R_{eff} by minimizing the RMSE (Painter
 255 et al., 2009).

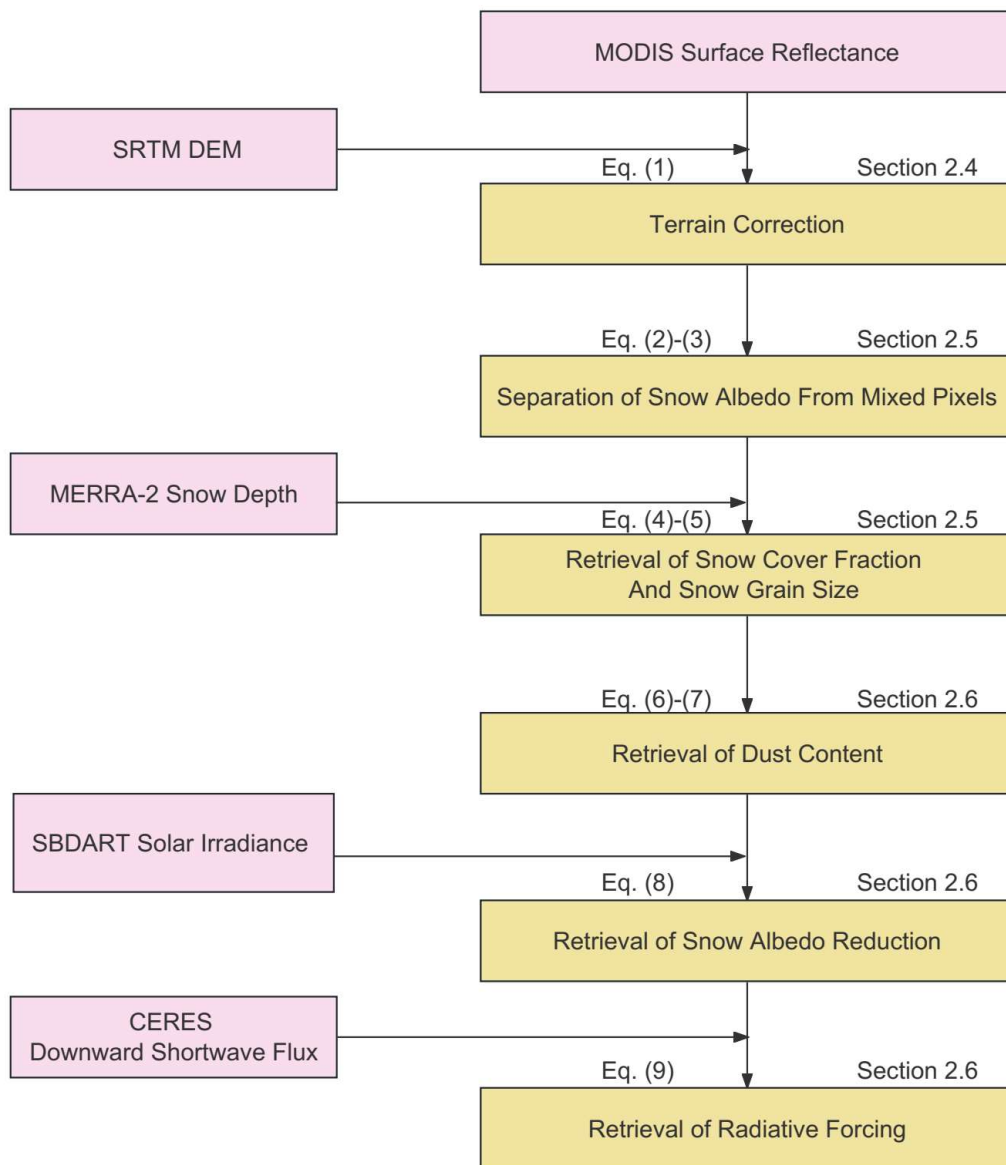


Figure 2. Flowchart illustrating the step-by-step retrieval of dust content and the associated snow albedo reduction and radiative forcing: the pink boxes denote the external input data, while the yellow boxes are used for calculations in this study.

2.6 Dust content and snow albedo reduction retrieval

We fit the SNICAR-simulated snow reflectance to the MODIS-derived snow reflectance in bands 3 and 4, which are the most sensitive to the dust content in snow, following Pu et al. (2019) and Cui et al. (2021), which are expressed as either

$$\text{RMSE} = \left(\frac{1}{2} \left((R_{\text{band 3}}^{\text{SNICAR, snow}} - R_{\text{band 3}}^{\text{MODIS, snow}})^2 + (R_{\text{band 4}}^{\text{SNICAR, snow}} - R_{\text{band 4}}^{\text{MODIS, snow}})^2 \right) \right)^{\frac{1}{2}} \quad (6)$$

or

$$\text{RMSE} = \left(\frac{1}{2} \left((R_{\text{band 3}}^{\text{SNICAR, snow}} - \left(\frac{R_{\text{band 3}}^{\text{MODIS}} - (1 - \text{SCF}) \times R_{\text{band 3}}^{\text{soil}}}{\text{SCF}} \right))^2 + (R_{\text{band 4}}^{\text{SNICAR, snow}} - \left(\frac{R_{\text{band 4}}^{\text{MODIS}} - (1 - \text{SCF}) \times R_{\text{band 4}}^{\text{soil}}}{\text{SCF}} \right))^2 \right) \right)^{\frac{1}{2}}, \quad (7)$$

where $R_{\text{band 3}}^{\text{SNICAR, snow}}$ is a function of four factors: dust content, R_{eff} , snow depth, and solar zenith angle. The latter three factors have been derived, leaving the dust content as the only unknown. Therefore, the dust content can be retrieved by minimizing Eq. (7). We assume that the derived dust content in this study accounts for the total light absorption by all of the LAPs that are present in the snowpack. This is because our study area is close to the Taklamakan Desert (TD), where large amounts of dust accumulate on the snow surface annually. In contrast, anthropogenic activities and biomass burning are rare, resulting in limited depositions of black carbon (BC) and organic carbon (OC) (Fig. S8). Observations from snow and atmosphere have confirmed this phenomenon (Wake et al., 1994; Huang et al., 2007). Therefore, our assumption is plausible.

The dust-induced broadband albedo reduction ($\Delta\alpha$) can then be calculated as follows:

$$\Delta\alpha = \frac{\sum_{\lambda=300\text{nm}}^{\lambda=2500\text{nm}} E_{\lambda} \cdot (R_{\lambda}^{\text{SNICAR, pure-snow}} - R_{\lambda}^{\text{SNICAR, snow}}) \cdot \Delta\lambda}{\sum_{\lambda=300\text{nm}}^{\lambda=2500\text{nm}} E_{\lambda} \cdot \Delta\lambda}, \quad (8)$$

Where $R_{\lambda}^{\text{SNICAR, pure-snow}}$ and $R_{\lambda}^{\text{SNICAR, snow}}$ are the SNICAR-simulated pure and

282 polluted snow albedo using snow grain size and dust content retrieved above, solar
283 zenith angle from MODIS and snow depth from MERRA2, respectively. E_{λ} represents
284 the spectral total solar irradiance at wavelength λ simulated from the SBDART model,
285 $\Delta\lambda$ is 10 nm, and $R_{\lambda}^{\text{SNICAR, pure-snow}}$ and $R_{\lambda}^{\text{SNICAR, snow}}$ are the SNICAR-simulated pure
286 and polluted snow albedo, respectively. The spectral irradiance from SBDART is only
287 used for integrating the spectral MODIS albedo to achieve broadband albedo. Thus, the
288 uncertainty in solar irradiance from the assumed atmospheric properties has limited
289 influence on the retrieval of snow albedo reduction (Cui et al., 2021).

290 The dust-induced radiative forcing (RF) is calculated as follows:

$$291 \text{RF} = \Delta\alpha \cdot \text{SW}, \quad (9)$$

292 where SW is the downward shortwave flux, which is obtained from CERES.

293 The in situ dust content was not measured to verify the MODIS retrievals because of
294 the challenging geographical conditions surrounding the TD. Nevertheless, Cui et al.
295 (2021) verified a similar retrieval method across the Northern Hemisphere. They
296 considered that the accuracy of MODIS surface reflectance is typically $\pm (0.005 + 0.05$
297 \times reflectance) under conditions where aerosol optical depth (AOD) is less than 5.0, and
298 solar zenith angle is less than 75° , as stated in the MODIS Surface Reflectance user's
299 guide (Collection 6; <https://modis.gsfc.nasa.gov/data/dataproduct/mod09.php>, last access:
300 19 January, 2024). In addition, the bias for snow grain size retrieval was assumed to be
301 30 % according to the studies of Pu et al. (2019) and Wang et al. (2017). These biases
302 led to an overall uncertainty ranging from 10% to 110% in the retrieval of LAPs across
303 the Northern Hemisphere. The study revealed that uncertainty decreased as LAPs
304 concentration increased, with reported uncertainties dropping to below approximately
305 30% in regions of high pollution, such as Northeast China. In our study, the snowpack
306 was also significantly polluted due to severe dust depositions, leading us to consider a
307 retrieval uncertainty of 30% for LAPs, in alignment with the findings of Cui et al.
308 (2021). Then, the overall lower bound and upper bound of the uncertainty value of snow
309 albedo reduction retrieval was calculated and will be discussed in the following section.
310 Moreover, we utilized the LAPs and the corresponding albedo reduction retrieved at

311 the local time of 10:30 AM (the time of the MODIS Terra satellite overpass), as the
312 proxy for daily averages following Painter et al. (2012). This approximation was
313 reasonable, given that the content of LAPs exhibited little variation over a diurnal cycle
314 (Painter et al., 2009; Zege et al., 2011). The variation in snow albedo throughout the
315 day was primarily attributed to changes in the solar zenith angle (Figure S1). Since the
316 solar zenith angle predominantly influences snow albedo in NIR, with little impact on
317 the VIS, the diurnal variation in LAPs-induced snow albedo reduction was also
318 considered limited.

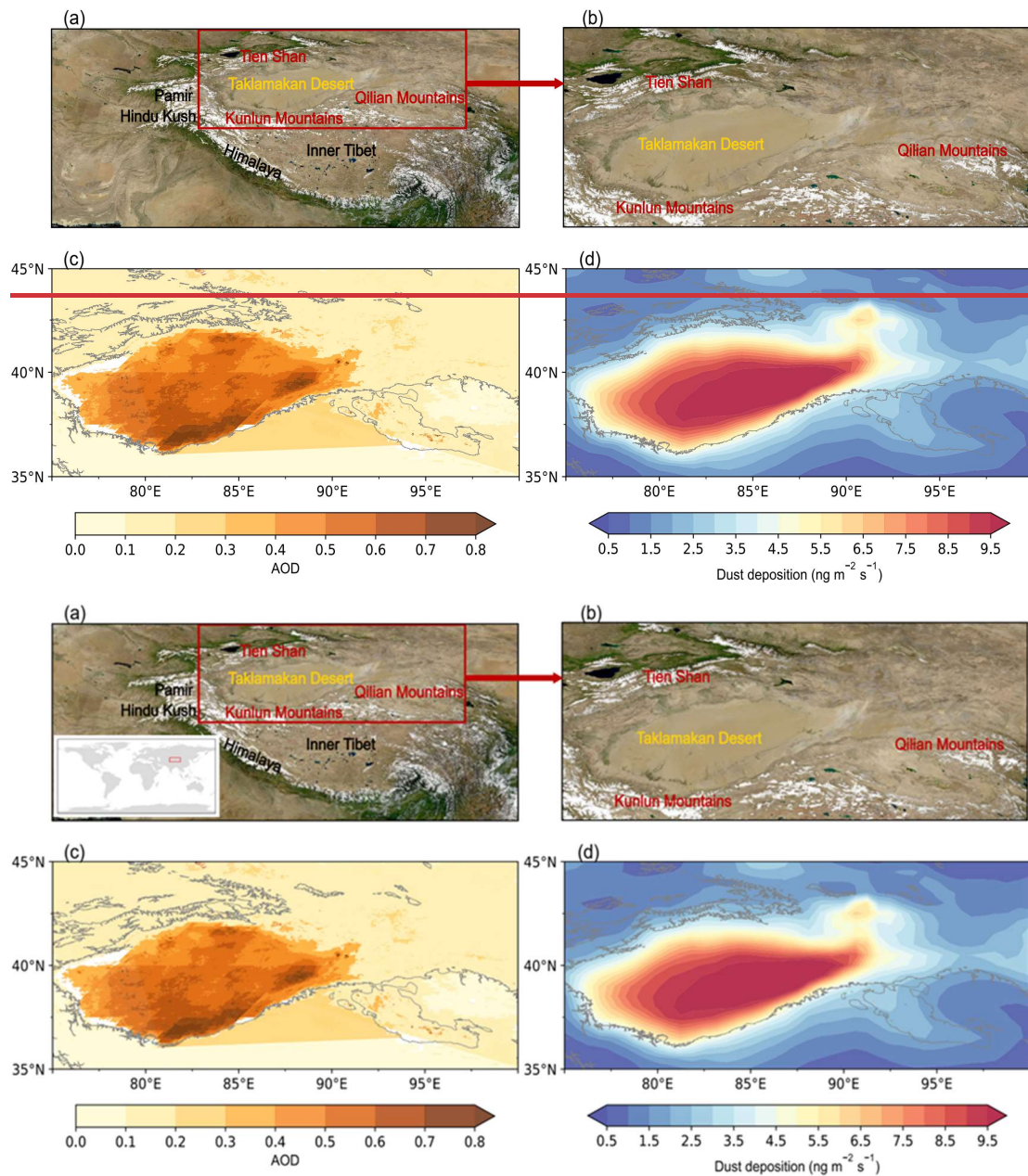
319 ~~and reported an uncertainty of less than ~40% over highly polluted snow.~~ As noted
320 above, the snow albedo reduction is mainly dependent on the dust content, R_{eff} , snow
321 depth, and solar zenith angle. The R_{eff} and snow depth can be categorized as snow
322 properties. We compared the dust content, snow properties, and solar zenith angle to
323 discuss their contributions to the spatial variations in snow albedo reduction (Pu et al,
324 2019; Cui et al., 2021). The supplementary information contains a thorough derivation
325 of this method.

326 **3 Results**

327 **3.1 Remote sensing of the snow darkening effect across the high mountains** 328 **surrounding the TD**

329 The TD is located in the northern part of HMA and is surrounded by some of the highest
330 mountain ranges on Earth, including the Kunlun Mountains, Tien Shan, and Pamir
331 (Figures [2a-3a](#) and b). The TD region emits vast amounts of dust particles into the
332 atmosphere each year, particularly during the spring and summer (Wang et al., 2008;
333 Chen et al., 2013, 2017b; Kang et al., 2016; Wu et al., 2021; Tang et al., 2022); this
334 phenomenon is confirmed by the high AOD levels at 550 nm from March to August
335 (Figure [_23c](#)). A significant amount of this dust is ultimately redeposited across the
336 Tarim Basin and the surrounding mountains. The Tien Shan and Kunlun Mountains are
337 two regions that experience high levels of dust deposition owing to the local topography
338 and atmospheric circulation patterns (Figure [2d3d](#)) (Huang et al., 2007, 2014; Ge et al.,
339 2014; Dong et al., 2022). Therefore, we selected two typical cases to demonstrate the

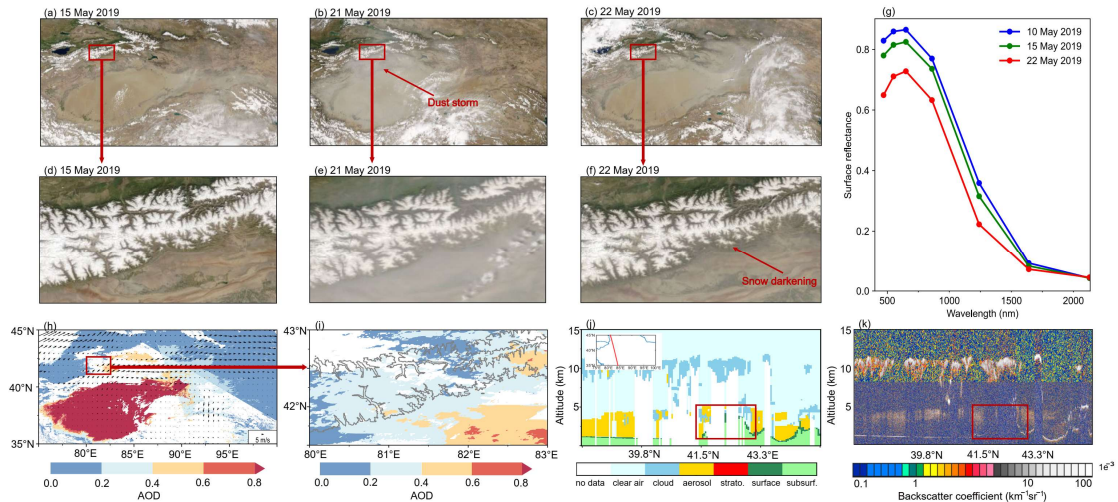
340 snow-darkening effect across the mountains surrounding the TD, a springtime dust
341 event across the Tien Shan and a summertime dust event across the Kunlun Mountains.



343
344 **Figure 23.** Mountain ranges surrounding the Taklamakan Desert, and AOD and
345 dust deposition distributions across the Taklamakan Desert and surrounding
346 region. (a, b) Geographic location of the Taklamakan Desert and surrounding
347 mountains. The red box defines the area in (b). Spatial distributions of the
348 averaged (c) AOD and (d) dust deposition values, which were derived from
349 MCD19A2 and MERRA-2 during the March to August 2019 period.

350 **3.1.1 Dust-induced snow darkening across the Tien Shan**

351 A significant dust storm occurred across the TD region on 18–22 May 2019 (Figures 4
352 and S2). The 21 May 2019 Terra/MODIS satellite image (Figure 3b4b) showed that the
353 dust plumes had spread to the north and east owing to an upper anticyclone system in
354 the Tarim Basin (Figure 3h4h). Some dust particles were uplifted to >4 km altitude, as
355 shown in the CALIPSO aerosol vertical profiles (Figures 3j-4j and k). These dust
356 particles were then transported to the snow-covered high-elevation areas of the Tien
357 Shan, as illustrated in the MODIS AOD images (Figures 3h-4h and i). Dust plumes
358 were also observed in a satellite image that spanned the broadly snow-covered central
359 Tien Shan (Figure 3e4e), and the snow appeared to darken in the 22 May 2019
360 Terra/MODIS satellite image that was acquired under the first clear-sky conditions after
361 this severe dust event. However, the snow was much whiter prior to the passage of this
362 dust storm, as shown in Figures 3d-4d and f. Figure 3g-4g further illustrates changes in
363 the surface reflectance of the snow-covered areas, providing a more intuitive influence
364 of dust deposition on the snow physical properties. The reflectance was around 0.8 in
365 the VIS spectrum on 15 May 2019, but quickly decreased to <0.7 on 22 May 2019, after
366 the passage of the dust plumes. The reduction in VIS wavelengths was up to >0.1 during
367 this short time interval. These observations show that the dust plumes from the TD can
368 significantly darken the snowpack across the Tien Shan through heavy dust deposition.
369 Furthermore, the progression of air-temperature-induced snow aging cannot effectively
370 explain this phenomenon. This result is consistent with previous satellite observations
371 over the Himalayas (Gautam et al., 2013).

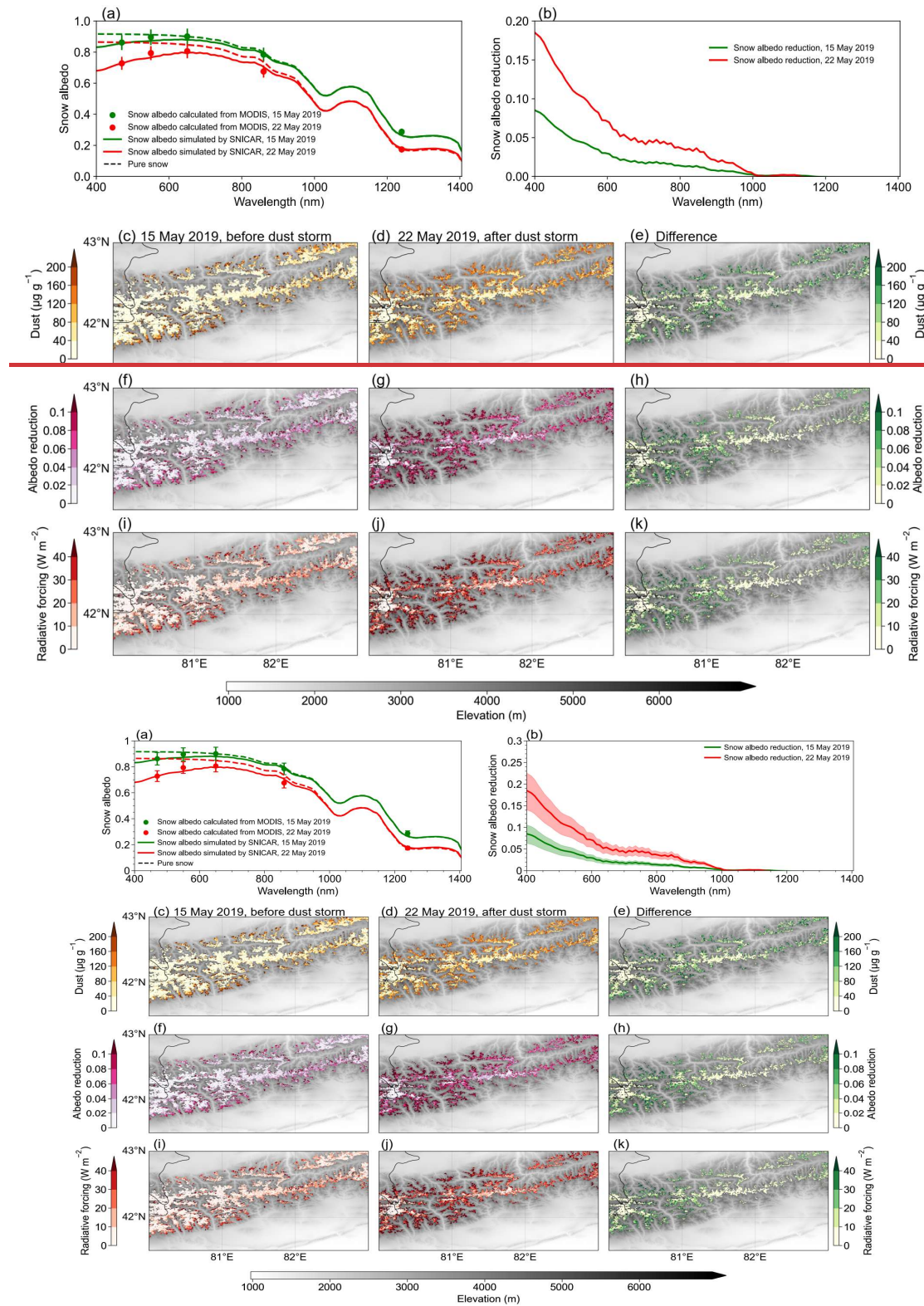


372

373 **Figure 34.** Satellite observations during the 18–22 May 2019 severe dust event
 374 across the Tien Shan. (a, d) Terra/MODIS satellite true-color images acquired on
 375 15 May 2019, prior to the dust storm. (b, e) Terra/MODIS satellite images
 376 acquired on 21 May 2019, with the dust storm transport from the TD to the Tien
 377 Shan indicated by the red arrow in (b). (c, f) Terra/MODIS satellite images
 378 acquired on 22 May 2019, with significant snow darkening observed across the
 379 Tien Shan after the dust storm. (g) MOD09GA spectral surface reflectance across
 380 snow-covered areas on 10 May 2019 (blue), 15 May 2019 (green), and 22 May 2019
 381 (red). (h) MODIS AOD image on 21 May 2019, with the ERA5 daily mean wind
 382 vector at 700 hPa overlain. (i) MODIS AOD image across the Tien Shan on 21
 383 May 2019. Gray lines denote the 3000 m elevation contour. CALIPSO (j) vertical
 384 feature mask and (k) backscatter coefficient on 21 May 2019.

385 We also derived the spectral snow albedo and retrieved several parameters to
 386 quantitatively assess the impact of this dust deposition on snow darkening. The
 387 SNICAR-simulated spectral snow albedo (solid lines) and MODIS-derived 5-band
 388 snow albedo (dots) in Figure 4a–5a are averaged over the area in Figure 4e5c. These
 389 results demonstrate an agreement of >95%, thereby indicating the reliability of our
 390 retrievals. The spectral snow albedo reduction on 15 and 22 May 2019 are shown in
 391 Figure 4b5b. There were significant increases in the albedo reductions as the
 392 wavelength decreased, particularly on 22 May 2019, which is consistent with

393 theoretical simulations of the dust-induced snow darkening effect (Figure 1). However,
394 the spectral curve differed from the BC-induced results in the anthropogenically
395 influenced areas of Northeast China (Wang et al., 2017; Niu et al., 2022) and Northwest
396 China (Shi et al., 2020). Therefore, we indicate that the observed snow darkening in
397 this study was mainly caused by natural dust emissions, as opposed to BC and organic
398 carbon (OC) emissions from anthropogenic activities and/or biomass burning. There
399 was a spectral snow albedo reduction of 0.02–0.08 in the VIS on 15 May 2019, which
400 represents persistent but relatively low dust deposition during spring. However, the
401 severe dust event caused a rapid increase in spectral snow albedo reduction to 0.045–
402 0.18 in a matter of days. The approximate doubling of the albedo reduction indicates
403 that the increase in the dust concentration was much greater than 100% based on the
404 nonlinear theory of the snow albedo feedback to the dust concentration (Figure 1). This
405 implies that it is important to consider both the frequency and intensity of dust events
406 when examining their impact on snow albedo. Similar phenomena that were induced
407 by catastrophic wildfire events have been observed in the snowpack across New
408 Zealand (Pu et al., 2021). These results suggest that extreme events may reflect the
409 more pronounced impact of climate warming on our planet (Liang et al., 2021; Gui et
410 al., 2022). Therefore, it is important to pay more attention to extreme events, rather than
411 just conducting either annual or monthly averaged analyses, to fully capture the
412 influence of climate change on snow albedo.



413

414

415 **Figure 45.** (a) Averaged SNICAR-simulated spectral snow albedo (solid lines) and
 416 MODIS-derived 5-band snow albedo (dots) for the region across the Tien Shan
 417 impacted by the 18–22 May 2019 severe dust event. (b) Snow albedo reduction on
 418 15 May 2019 (green) and 22 May 2019 (red). Shadows indicate the retrieval

419 **uncertainty.** Spatial distributions of the average (c, d) dust, (f, g) albedo reduction,
420 and (i, j) radiative forcing on 15 and 22 May 2019, respectively. Spatial
421 distributions of the differences in (e) dust, (h) albedo reduction, and (k) radiative
422 forcing between 15 and 22 May 2019. The background image in (c–k) is a grayscale
423 topographic map of the Tien Shan.

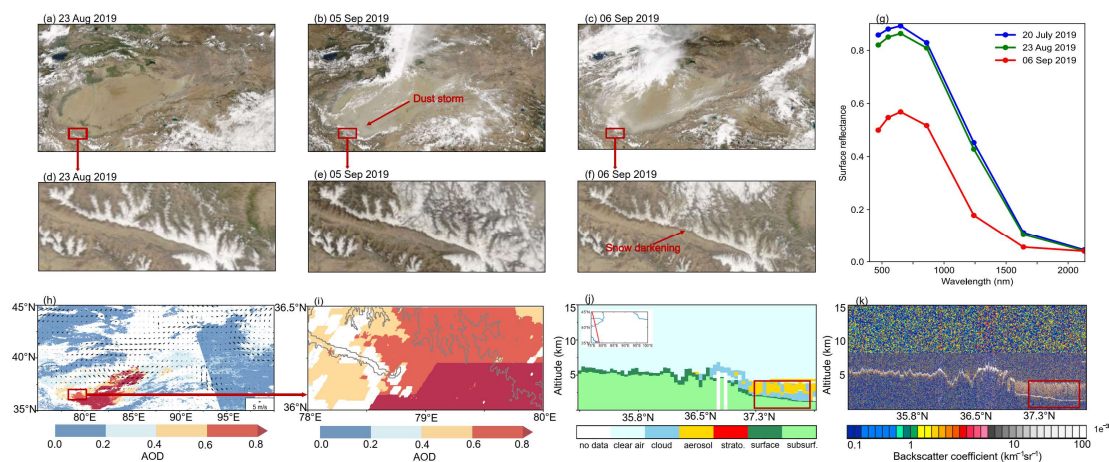
424 Figures 4e–5c and d illustrate the spatial distributions of the dust concentration in the
425 snowpack on 15 and 22 May 2019, respectively. There was a sharp increase in the dust
426 content from 2–55 to 42–192 $\mu\text{g g}^{-1}$ (~2.67-fold increase) following the severe dust
427 event, with the lower elevations possessing higher dust concentrations and greater dust
428 content increases (Figures 4d–5d, 5a and e and S3). Snow darkening was observed across
429 all of the snow-covered areas ($>2100 \text{ km}^2$), including the summits, thereby highlighting
430 the extensive influence of this severe dust event across the central Tien Shan.
431 Furthermore, these results demonstrate the capability and effectiveness of employing
432 satellite remote sensing to observe/monitor large-scale snow darkening. The dust-
433 induced broadband snow albedo reductions and radiative forcing are shown in Figures
434 4f–5f–k, with observed spatial patterns that are largely similar to the dust content
435 distributions. The snow albedo reduction increased by 0.008–0.052, with an observed
436 increase from 0.002–0.032 on 15 May to 0.028–0.079 on 22 May. The radiative forcing
437 increased by 2.5–20.5 W m^{-2} , with an observed increase from 0.5–12.5 W m^{-2} on 15
438 May to 11–31.5 W m^{-2} on 22 May (Figure S7S4). Both the snow albedo reduction and
439 radiative forcing increased by a factor of ~2.39, which directly reflects its significant
440 impact on the regional radiation balance and climate (Dumont et al., 2020). Snow
441 darkening can also accelerate snow aging by absorbing more shortwave radiation in a
442 warming spring, as characterized by the R_{eff} growth (Figures S3a–c). Figure S5a–d show
443 the overall uncertainty in snow albedo reduction retrieval in Tien Shan, with the
444 uncertainty bounds averaging 24% (-26%) on 15 May and 22% (-24%) on 22 May,
445 respectively. As the dust content increases, the uncertainty in the snow albedo reduction
446 decreases.

447

448 **3.1.2 Dust-induced snow darkening across the Kunlun Mountains**

449 The Kunlun Mountains are located along the southern (northern) edge of the Tarim
 450 Basin (Tibetan Plateau). The northern slope of the Central/West Kunlun Mountains
 451 directly faces the TD (Figure 1a) and should have experienced the most severe dust-
 452 induced snow darkening. Similar conditions also exist across the Himalayas, where the
 453 south slope faces both the Thar Desert in India and the Middle East. We captured a
 454 typical dust storm event with associated dust deposition and snow darkening that
 455 occurred between 5 and 11 May 2020 along the northern slope of the Kunlun Mountains
 456 using MODIS satellite images (Figure S2S6). The previously mentioned spring
 457 phenomenon is well-known due to intense springtime dust emissions from the TD,
 458 whereas the summer phenomenon is usually overlooked. However, it has been shown
 459 that dust can more effectively cross the Kunlun Mountains during the summer months,
 460 with the potential to induce changes in atmospheric dynamics and thermal effects (Yuan
 461 et al., 2018). Therefore, we specifically chose a summer case to highlight snow
 462 darkening across the Kunlun Mountains.

463

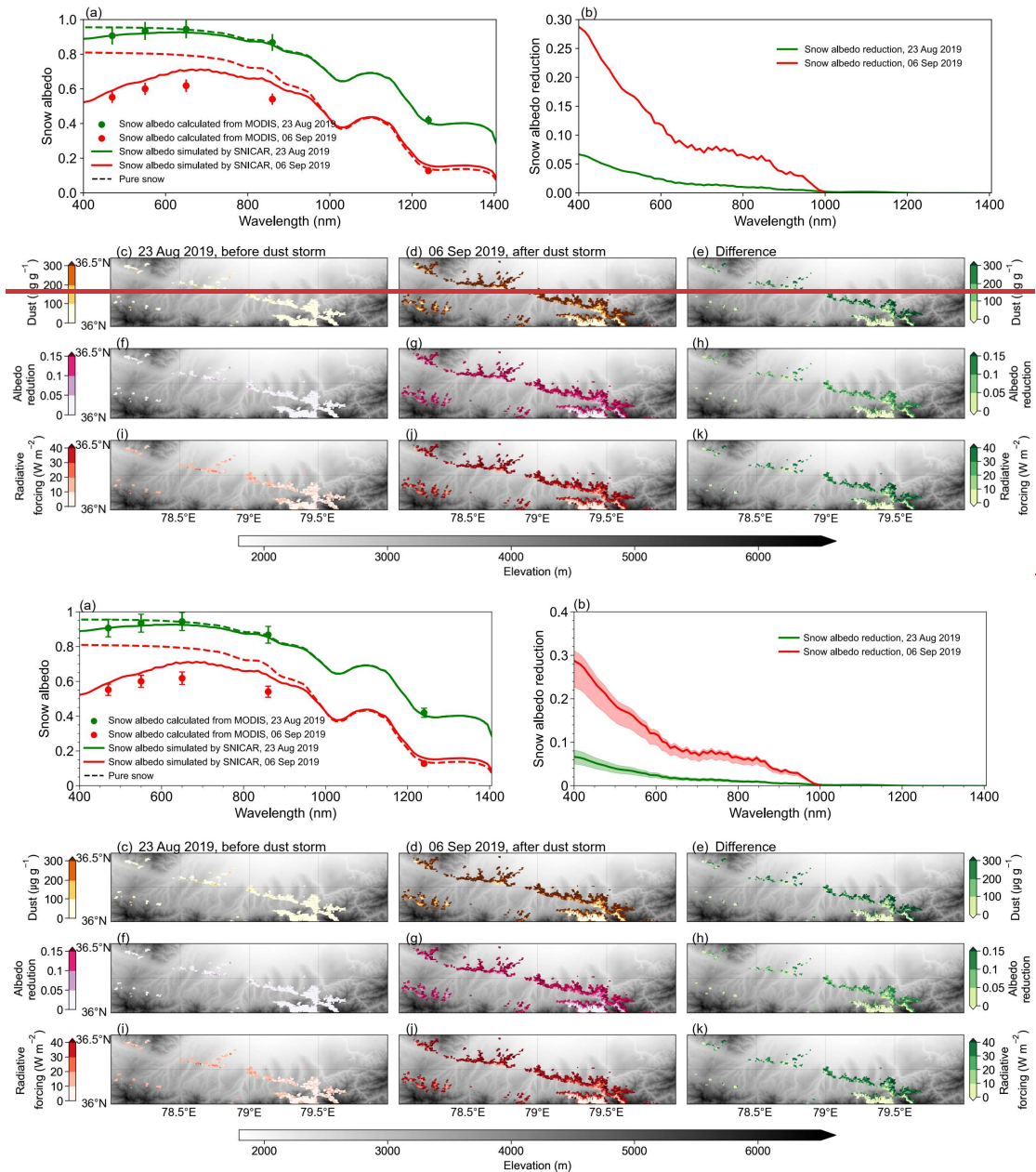


464

465 **Figure 56. Satellite observations during the 26 Aug to 08 Sep 2019 dust storm**
 466 **across the Kunlun Mountains. (a, d) Terra/MODIS satellite true-color images**
 467 **acquired on 23 Aug 2019, prior to the dust storm. (b, e) Terra/MODIS satellite**
 468 **images acquired on 05 Sep 2019, with the dust storm transport from the TD to the**
 469 **Kunlun Mountains indicated by the red arrow in (b). (c, f) Terra/MODIS satellite**
 470 **images acquired on 06 Sep 2019, with significant snow darkening across the**

471 **Kunlun Mountains after the dust storm. (g) MOD09GA spectral surface**
472 **reflectance over the snow-covered areas on 20 July 2019 (blue), 23 Aug 2019**
473 **(green), and 06 Sep 2019 (red). (h) MODIS AOD image on 05 Sep 2019, with the**
474 **ERA5 daily mean wind vector at 700 hPa overlain. (i) MODIS AOD image across**
475 **the Kunlun Mountains on 05 Sep 2019. Gray lines denote the 3000-m elevation**
476 **contour. CALIPSO (j) vertical feature mask and (k) backscatter coefficient on 04**
477 **Sep 2019.**

478 A significant dust event that impacted the northern slope of the Kunlun Mountains
479 occurred from 26 Aug to 08 Sep 2019 (Figures [5b6b](#) and [S7](#)). The Terra/MODIS
480 satellite images on 5 Sep 2019 (Figures [5b-6b](#) and [e](#)) show the accumulation of dust
481 plumes along the southern edge of the Tarim Basin. In summer, the westerlies weaken
482 and shift to the north, leading to more accumulation of dust locally instead of
483 transporting it eastward (Chen et al., 2017a; Yuan et al., 2018). Furthermore, the
484 enhanced sensible heat flux favors the southward transport of uplifted dust, leading to
485 cyclonic convergence at the surface and anticyclonic divergence at the top of the
486 troposphere above the TD (Figure [5h6h](#)). The synergistic effects of atmospheric
487 dynamic and thermal forcing can cause the dust plumes to be uplifted to ~5 km altitude
488 (Figures [5j6j-k](#)). This uplift effectively facilitated the dust plume ascent to the snow-
489 covered areas across the northern slope of the Kunlun Mountains (Figure [5e-6e](#) and [i](#)).
490 A comparison of the MODIS images that were acquired on 23 Aug and 6 Sep 2019
491 highlighted snow darkening after this severe dust storm (Figures [5d-6d](#) and [f](#)). The
492 surface reflectance decreased by ~0.22 in the VIS spectrum, decreasing from 0.285 on
493 23 Aug to ~0.065 on 5 Sep. These observations indicate that this summertime dust event
494 caused significant snow darkening across the Kunlun Mountains.



495

496

497 **Figure 67.** (a) Averaged SNICAR-simulated spectral snow albedo (solid lines) and
 498 MODIS-derived 5-band snow albedo (dots) for the region across the Kunlun
 499 Mountains impacted by the 26 Aug to 08 Sep 2019 severe dust event. (b) Snow
 500 albedo reductions on 23 Aug 2019 (green) and 06 Sep 2019 (red). Shadows indicate
 501 the retrieval uncertainty. Spatial distributions of the average (c, d) dust, (f, g)
 502 albedo reduction, and (i, j) radiative forcing on 23 Aug and 06 Sep 2019,
 503 respectively. Spatial distributions of the differences in (e) dust, (h) albedo
 504 reduction, and (k) radiative forcing between 23 Aug and 06 Sep 2019. The

505 **background image in (c–k) is a grayscale topographic map of the Kunlun**
506 **Mountains.**

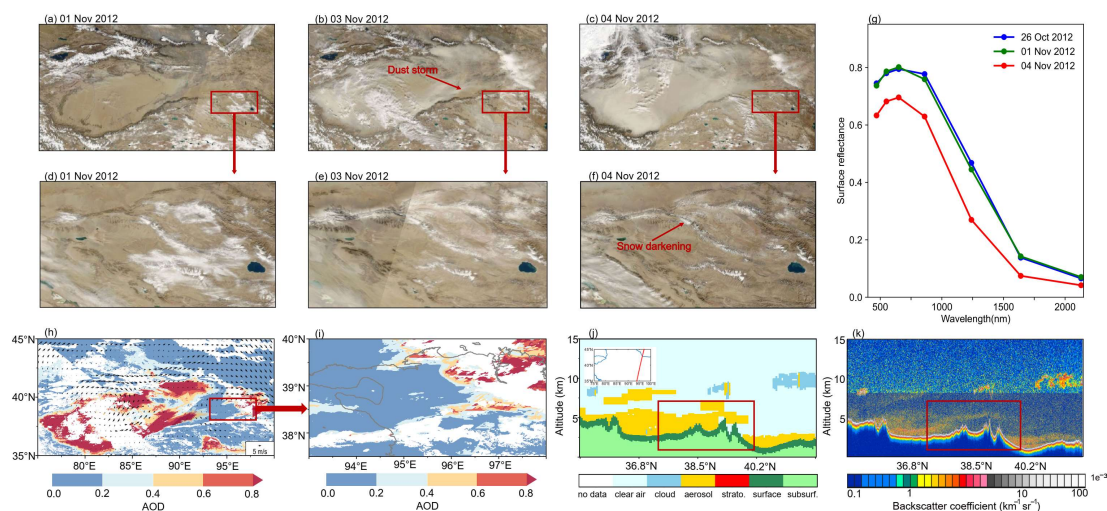
507 Figure 6-7 provides a more quantitative investigation of the impact of this severe dust
508 event on the snowpack across the Kunlun Mountains, whereby a significant increase in
509 dust content from 12–50 $\mu\text{g g}^{-1}$ on 23 Aug to 170–360 $\mu\text{g g}^{-1}$ on 06 Sep (~6.45-fold
510 increase) is observed after this severe dust event (Figure S8). The darkened snow-
511 covered area spans $>600 \text{ km}^2$, with a clear south–north gradient in the dust
512 concentration distribution that is influenced by both the orientation and elevation of the
513 mountains. This large dust deposition induced a 0.015–0.106 increase in snow albedo
514 reduction, with an observed increase from 0.013–0.032 on 23 Aug to 0.088–0.136 on
515 06 Sep. There was also a substantial increase in radiative forcing of 4.1–37.5 W m^{-2} ,
516 with an observed increase from 3–11 W m^{-2} on 23 Aug to 31–49 W m^{-2} on 06 Sep
517 (Figure S7S4). Note that these increases in both the snow albedo reduction and radiative
518 forcing are approximately two times larger than those observed over the Tien Shan
519 (Figure S3 and S8). These findings indicate accelerated snow aging, as evidenced by
520 the faster growth rate of the R_{eff} observed across the Kunlun Mountains (Figures S4 and
521 S5S9). Furthermore, Figure S5e-h show the overall uncertainty in snow albedo
522 reduction retrieval in Kunlun Mountains, with the uncertainty bounds averaging 23%
523 (-25%) on 23 Aug and 7% (-21%) on 06 Sep, respectively. Notably, compared to the
524 Tien Shan dust event described in Section 3.1.1, the Kunlun Mountains event
525 demonstrates a more significant reduction in the uncertainty of snow albedo reduction
526 as the dust content increases, especially in the upper bound of the uncertainty. This
527 observation aligns with findings reported by Cui et al. (2021).

529 **3.1.3 Snow darkening across the Qilian Mountains**

530 Unlike the Tien Shan and Kunlun Mountains, the Qilian Mountains are located
531 approximately 1000 km east of the Tarim Basin. The Hexi Corridor, a narrow and
532 relatively flat plain that lies between the high-elevation, inhospitable terrains of the
533 Mongolian and Tibetan plateaus (see Figure 23), is situated to the north of the Qilian

534 Mountains. The unique terrain of the region results in TD dust plumes following a
 535 preferred transport route across the Hexi Corridor to East Asia (Zhang et al., 2008;
 536 Meng et al., 2018). These dust plumes are generally uplifted to >4 km altitude and
 537 entrained in the westerlies (Huang et al., 2008; Dong et al., 2014; Chen et al., 2022),
 538 thereby providing a means for dust deposition onto the snowpack across the Qilian
 539 Mountains.

540



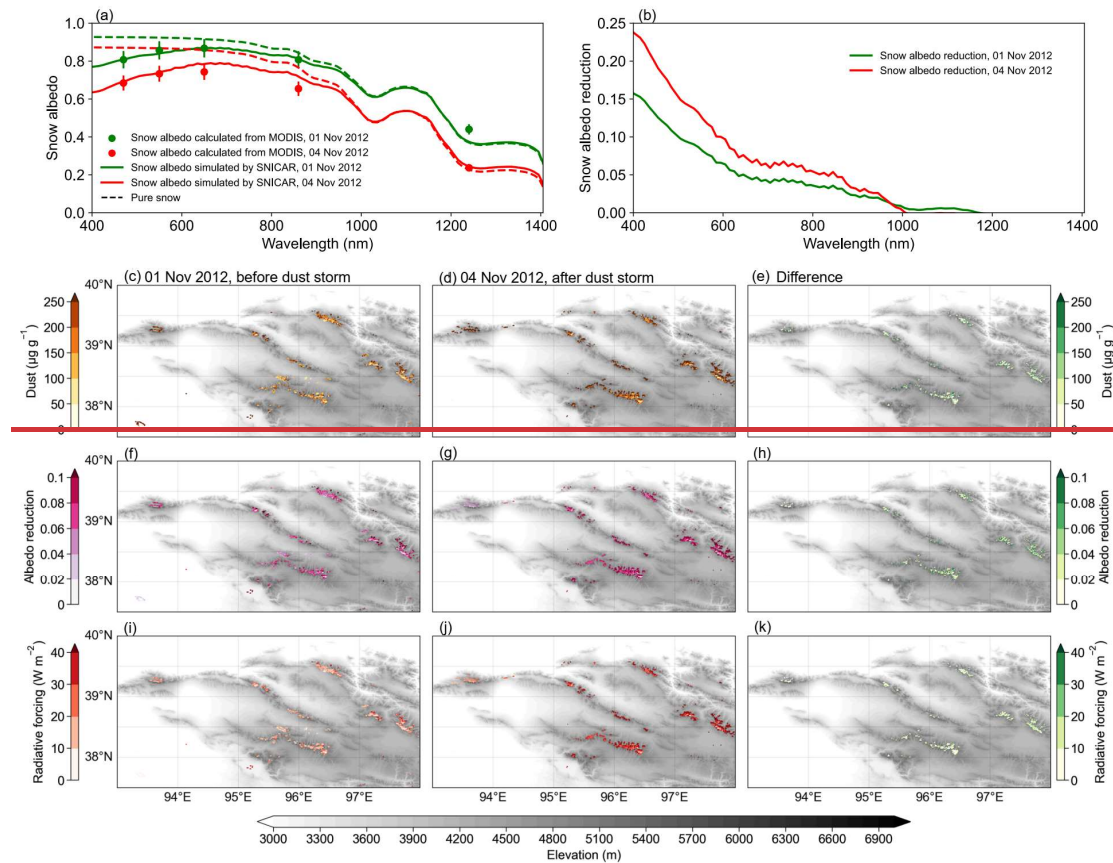
541

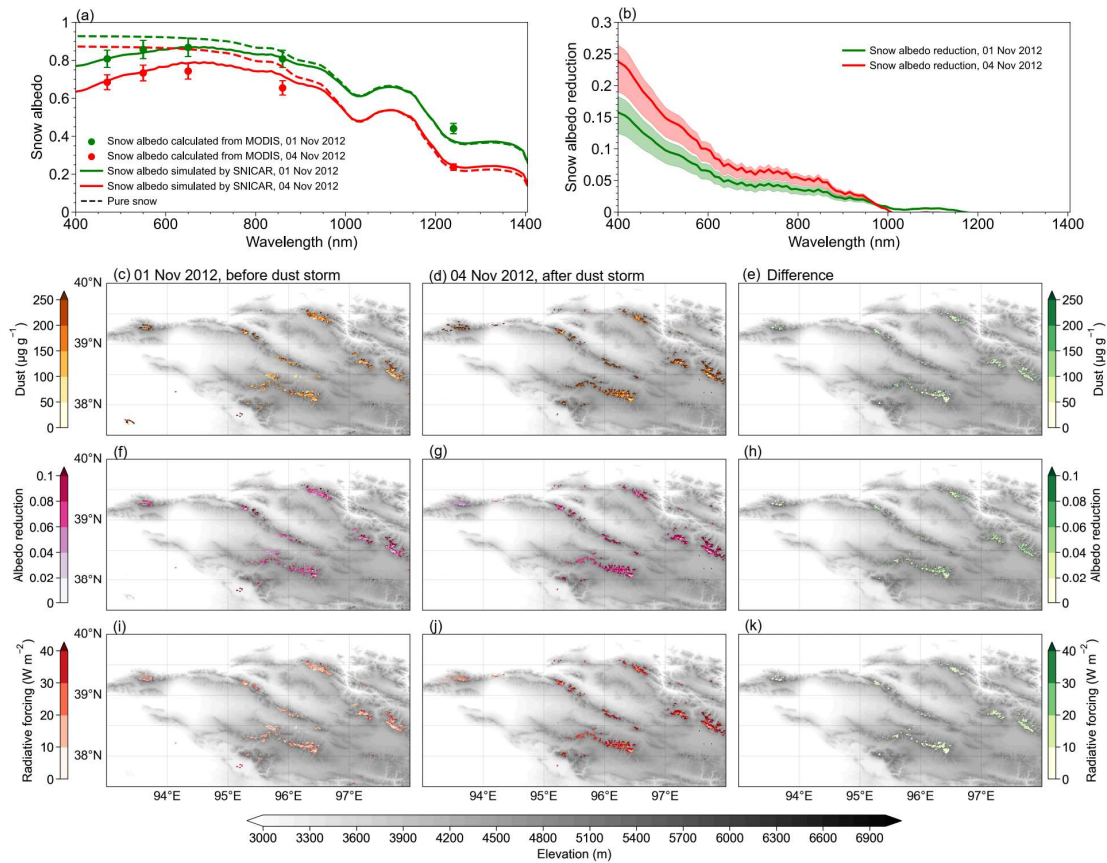
542 **Figure 7-8.** Satellite observations during the 02–04 Nov 2012 dust storm across the
 543 Qilian Mountains. (a, d) Terra/MODIS satellite true-color images acquired on 01
 544 Nov 2012, prior to the dust storm. (b, e) Terra/MODIS satellite images acquired
 545 on 03 Nov 2012, with the dust transport from the TD to the Qilian Mountains
 546 indicated by the red arrow in (b). (c, f) Terra/MODIS satellite images acquired on
 547 04 Nov 2012, with significant snow darkening observed across the Qilian
 548 Mountains after the dust storm. (g) MOD09GA spectral surface reflectance over
 549 the snow-covered areas on 26 Oct 2012 (blue), 01 Nov 2012 (green), and 04 Nov
 550 2012 (red). (h) MODIS AOD image on 03 Nov 2012, with the ERA5 daily mean
 551 wind vector at 700 hPa overlain. (i) MODIS AOD image across the Qilian
 552 Mountains on 03 Nov 2012. The gray line denotes the 3000-m elevation contour.
 553 CALIPSO (j) vertical feature mask and (k) backscatter coefficient on 03 Nov 2012.

554

Figure 7-8 illustrates a severe dust event that occurred from 02 to 04 Nov 2012_

555 (Figure S10), when abundant dust plumes were being transported across the narrow
 556 Hexi Corridor (Figures 7b-8b and h). The dust content was much more intense in this
 557 region, possessing AOD levels of up to >0.8. Furthermore, the CALIPSO
 558 observations indicated that the dust plumes were uplifted to ~10 km altitude (Figures
 559 7j-8j and k), thereby allowing some dust particles to cross over the northern slopes of
 560 the Qilian Mountains and spread across its western extent (Figures 7e-8e and i). The
 561 average reflectance in the VIS spectrum was stable at around 0.7–0.8 across the snow-
 562 covered areas about a week before the severe dust event but then significantly
 563 decreased to 0.6–0.7 owing to heavy dust deposition





565

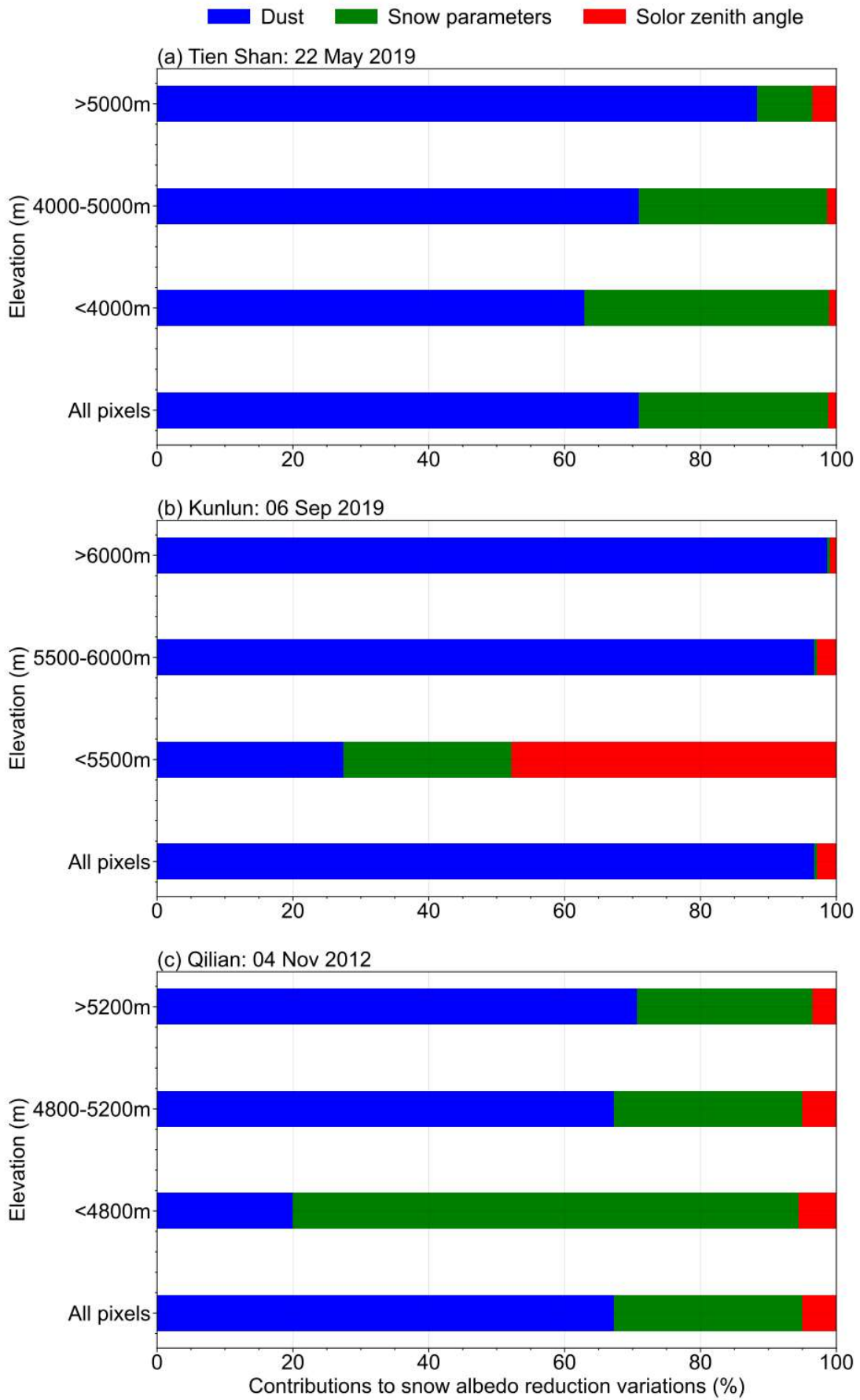
566 **Figure 89.** (a) Averaged SNICAR-simulated spectral snow albedo (solid lines) and
 567 MODIS-derived 5-band snow albedo (dots) for the region across the Qilian
 568 Mountains impacted by the 02–04 Nov 2012 severe dust event. (b) Snow albedo
 569 reductions on 01 Nov 2012 (green) and 04 Nov 2012 (red). **Shadows indicate the**
 570 **retrieval uncertainty.** Spatial distributions of the average (c, d) dust, (f, g) albedo
 571 reduction, and (i, j) radiative forcing on 01 and 04 Nov 2012, respectively. Spatial
 572 distributions of the differences in (e) dust, (h) albedo reduction, and (k) radiative
 573 forcing between 01 and 04 Nov 2012. The background image in (c–k) is a grayscale
 574 image of the Qilian Mountains.

575 Figure 8–9 presents the quantitative satellite-derived results, which highlight a rapid
 576 increase in dust content from 110–228 to 194–360 $\mu\text{g g}^{-1}$ (~1.53-fold increase) that
 577 spanned a snow-covered area of $>630 \text{ km}^2$ (Figures 89f–h). This significant increase
 578 in dust content led to a considerable increase in snow albedo reduction (radiative
 579 forcing) of 0.018–0.067 (3–16 W m^{-2}), which increased from 0.042–0.076 (11–20 W
 580 m^{-2}) on 1 Nov 2012 to 0.092–0.153 (22–38 W m^{-2}) on 4 Nov 2012 (Figure S7S4).

581 This >1.5-fold increase in snow albedo reduction (radiative forcing) was not solely due
582 to the deposition of dust (Figure S11). Accelerated snow aging, which was observed
583 from the enhanced R_{eff} growth (Figure S6S9), also contributed to the observed increase
584 in snow albedo reduction (radiative forcing); this trend was similar to that observed
585 across the Kunlun Mountains. Figure S5i-1 show the overall uncertainty in snow albedo
586 reduction retrieval in Qilian Mountains, with the uncertainty bounds averaging 16% (-
587 21%) on 01 Nov and 11% (-20%) on 04 Nov, respectively. Our approach uses satellite
588 remote sensing to obtain a more complete spatiotemporal evolution of the TD dust
589 storm, including its emission, long-range transport, and deposition, across the Qilian
590 Mountains, which offers advantages over previous field measurements (Wei et al.,
591 2017).

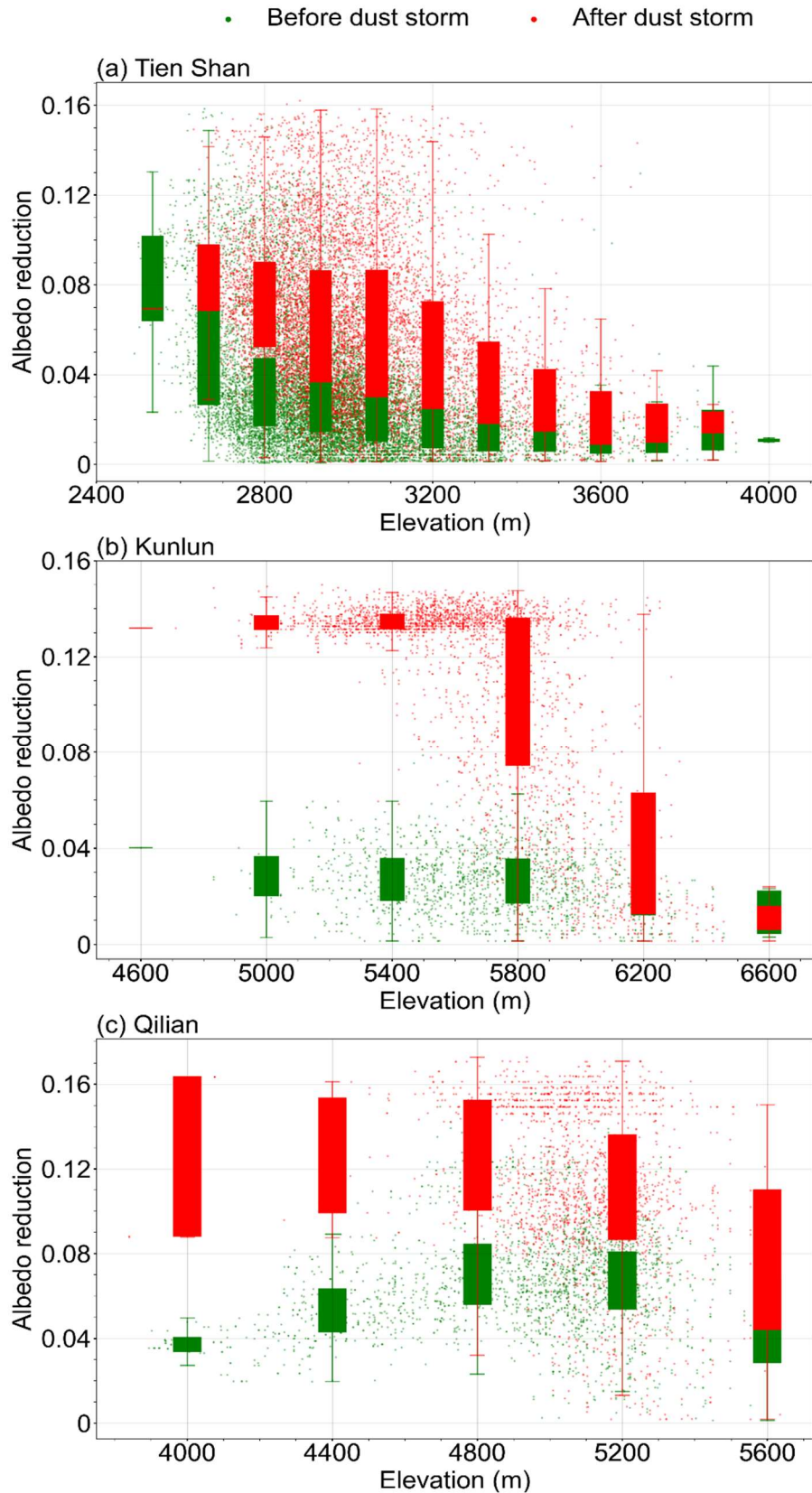
593 **3.2 Contributions to the spatial and altitudinal variations in dust-induced snow** 594 **darkening**

595 We quantified the contributions of the three key factors (dust content, snow properties,
596 and solar zenith) to the spatial variations in snow albedo reduction (Figure 910) using
597 the method described in Section 2.6. The dust content was the dominant contributor to
598 the spatial variations in snow darkening. This is at least partially attributed to the greater
599 spatial differences in dust content compared with those of the other factors, as shown
600 in Figures 45, 67, and 89. Furthermore, theoretical modeling has indicated that the snow
601 albedo reduction is more sensitive to changes in dust content than to changes in the
602 snow properties and solar zenith angle (Flanner et al., 2021; Usha et al., 2022; Zhao et
603 al., 2022). Laboratory experiments also support these findings (Zhang et al., 2018; Li
604 et al., 2022). The contribution of the dust content also increased as the elevation in each
605 mountain range increased, whereas a decreasing trend was observed for the snow
606 parameters. This is because the dust content exhibits spatial differences across all of the
607 elevations owing to its widespread and heterogeneous depositions. However, the snow
608 depth has a more semi-infinite nature and R_{eff} exhibits greater spatial homogeneity at
609 higher elevations owing to slower snow aging.



611 **Figure 910. Contributions of the spatial variations in dust content (blue), snow**
612 **parameters (green), and solar zenith angle (red) to the snow albedo reduction at**
613 **different elevations across the (a) Tien Shan, (b) Kunlun Mountains, and (c) Qilian**
614 **Mountains.**

615 Scatter plots of the snow albedo reduction for the elevations across the Tien Shan,
616 Kunlun Mountains, and Qilian Mountains are shown in Figure 1011. The snow albedo
617 reduction across the Tien Shan decreased with increasing elevation prior to the dust
618 storm. However, the most severe dust deposition occurred within the 4000–4500 m
619 elevation range, resulting in the most significant enhancement of snow albedo reduction
620 in this elevation range. These findings are consistent with those reported for the
621 Himalayas (Sarangi et al., 2020). The snow albedo reduction was generally low across
622 the Kunlun Mountains for all of the elevation ranges. However, dust deposition caused
623 the most significant albedo reduction within the 4500–5500 m elevation range, with a
624 dramatic decrease of its influence above 6000 m. These findings correspond to the
625 CALIPSO aerosol vertical profile observations (Figures 5j–6j and k). The snow albedo
626 reduction across the Qilian Mountains initially increased with elevation up to ~5000 m
627 and then decreased at high elevations prior to the dust storm. However, the most severe
628 dust deposition occurred across the lower elevations, leading to the most significant
629 enhancement of snow albedo reduction across these lower-elevation regions. Our
630 elevation analysis revealed a consistent outcome, whereby the dust storms significantly
631 darkened the snowpack up to >5000 m elevation across the three analyzed mountain
632 ranges.



633

634

Figure 1011. Scatter plots of the snow albedo reductions for the analyzed elevation ranges across the (a) Tien Shan, (b) Kunlun Mountains, and (c) Qilian Mountains.

635

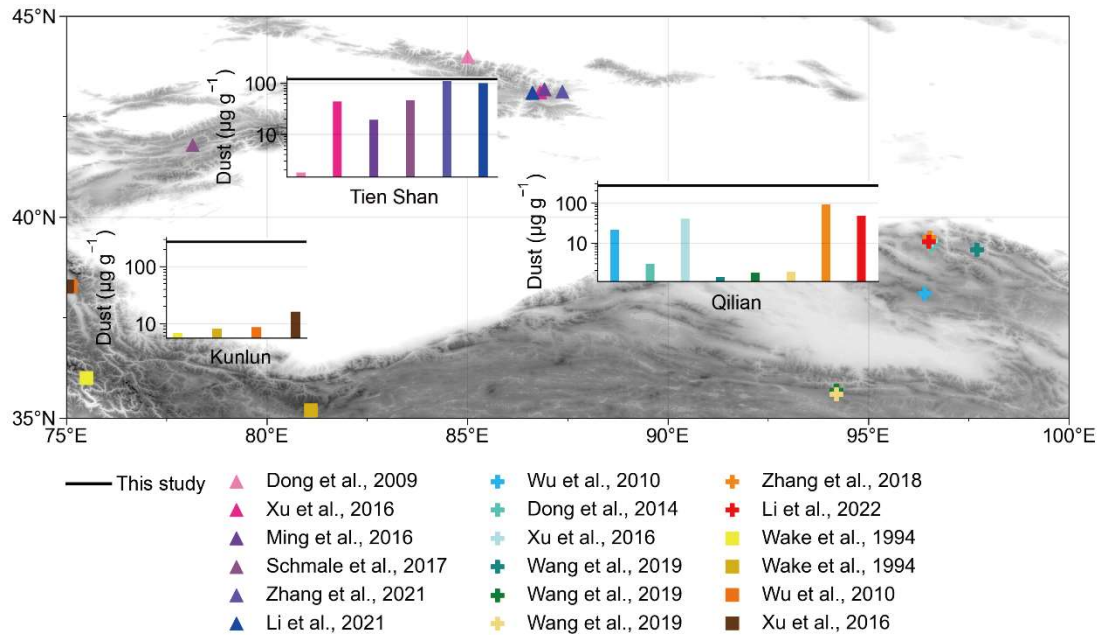
636

Each box plot shows the statistical results for a 400-m elevation interval.

637 **4 Discussion**

638 The snow darkening effect and its resultant radiative forcing have gained increasing
639 attention in recent decades owing to their significant impacts on regional climate and
640 hydrological systems. However, studies in the Tien Shan, Kunlun Mountains, and
641 Qilian Mountains have been limited to local-scale observations, despite the significant
642 impact of dust on snow darkening in these regions. Here we provide an overview of
643 previous in situ dust-content measurements in the snowpack across the study region for
644 comparison with our satellite remote-sensing results (see Figure [H12](#)). In the Tien Shan
645 region, Ming et al. (2016), Xu et al. (2016), Li et al. (2021), and Zhang et al. (2021)
646 reported a dust content of 19.3–110 $\mu\text{g g}^{-1}$ in the snowpack across Urumqi Glacier No.1.
647 Dong et al. (2009) observed an average dust content of 0.97–3.69 $\mu\text{g g}^{-1}$ in the
648 snowpack across Urumqi Glacier No. 1, Haxilegen Glacier No. 51, and Miaoergou
649 Glacier. Schmale et al. (2017) found a variable dust content of 68.1–125.9 $\mu\text{g g}^{-1}$ in the
650 snowpack across Suet Zapadny, No. 354, and Golubin glaciers in the western Tien
651 Shan. In the Kunlun Mountains, Wake et al. (1994) reported a dust content of up to ~ 8
652 $\mu\text{g g}^{-1}$ in the snow/ice across the western Kunlun Mountains. Wu et al. (2010) and Xu
653 et al. (2016) measured dust contents of ~ 8.68 and 16.24 $\mu\text{g g}^{-1}$ in the ice core and
654 snowpack across Muztagata Glacier in the northwestern Tibet Plateau (Wu et al., 2010;
655 Xu et al., 2016), respectively. In the Qilian Mountains, Wu et al. (2010) analyzed ice
656 cores from Dunde Glacier and measured a dust content of ~ 21 $\mu\text{g g}^{-1}$. The measured
657 dust contents in the snowpack across Laohugou Glacier ranged from around 3 to 93.2
658 $\mu\text{g g}^{-1}$ (Dong et al., 2014; Xu et al., 2016; Zhang et al., 2018; Li et al., 2022). Wang et
659 al. (2019) measured a variable dust content of 1.4–1.9 $\mu\text{g g}^{-1}$ in the fresh snow across
660 Qiyi, Meikuang, and Yuzhufeng glaciers. Overall, previous field studies have reported
661 dust contents of 0.97–125.9, 6.78–16.24, and 1.4–93.2 $\mu\text{g g}^{-1}$ for the Tien Shan, Kunlun
662 Mountains, and Qilian Mountains, respectively.

663



664

665 **Figure H12. Comparisons of the satellite-derived dust contents (black lines) in**
 666 **snow from this study and observed values from previous studies (colored symbols**
 667 **and bars).**

668 Our satellite-derived approach has yielded much higher dust contents than those
 669 obtained via in situ field measurements, with 42–196, 170–360, and 194–360 $\mu\text{g g}^{-1}$
 670 determined for the Tien Shan, Kunlun Mountains, and Qilian Mountains, respectively.

671 A key reason for this discrepancy could be that the field measurements usually record
 672 the background dust content signal, which includes a gradual natural deposition of dust,
 673 whereas our analysis specifically focused on significant snow darkening events due to
 674 severe dust storms, which further highlights the advantage of employing remote-
 675 sensing techniques to observe extreme snow darkening phenomena (Li et al., 2020).

676 We do note that satellite-derived approaches possess their own uncertainties, which
 677 arise from the data resolution and accuracy, algorithm assumptions, and atmospheric
 678 and underlying surface interferences (Cui et al., 2021). Nevertheless, this satellite-
 679 derived approach remains a valuable tool for effectively and rapidly studying extreme
 680 events, which cannot be captured by field measurements or climate model simulations,
 681 particularly as these extreme events will become increasingly important for climate and
 682 hydrological systems as the global climate continues to warm (Clow et al., 2016;
 683 Dumont et al., 2020).

684 Given the significant snow darkening effect highlighted in this study and recent
685 observations of decreasing snow cover across the Tien Shan, Kunlun Mountains, and
686 Qilian Mountains (She et al., 2015; Li et al., 2020; Zhu et al., 2022), it is crucial to
687 evaluate the impact of snow darkening on regional hydrologic cycles and local
688 freshwater supplies. However, snow aging and melting mechanisms are complex and
689 therefore require complementary observations because remote sensing alone cannot
690 distinguish the influences of augmented shortwave radiation owing to dust and
691 increased air temperatures on snow aging and melting (Gautam et al., 2013). Additional
692 research that integrates model simulations and satellite observations is necessary to
693 differentiate the roles of snow darkening and global warming in enhancing snow aging
694 and melting, and the resultant changes in glacier runoff in the future.

695 **5 Conclusions**

696 Our study focused on the impact of the annual vast dust emissions from the Taklamakan
697 Desert on the surrounding high mountain snowpack. Using a combination of MODIS
698 satellite data analysis and SNICAR model simulations, we aimed to reveal significant
699 snow-darkening events and quantify the resulting snow albedo reduction and radiative
700 forcing caused by severe dust storms. Our analysis of the satellite data revealed
701 significant snow darkening over the 3000–6000 m elevation range across the Tien Shan
702 and Kunlun Mountains. This phenomenon was attributed to the high uplift of dust
703 owing to the local topography and atmospheric circulation. The impacted area,
704 spanning the track of the dust storm, encompassed almost all of the snow-covered areas
705 across the Tien Shan (>2100 km²) and Kunlun Mountains (>600 km²), including the
706 summits. The dust content in the snowpack increased to 42–192 and 170–360 μg g⁻¹,
707 resulting in significant increases in snow albedo reduction (radiative forcing) of 0.028–
708 0.079 (11–31.5 W m⁻²) and 0.088–0.136 (31–49 W m⁻²) across the Tien Shan and
709 Kunlun Mountains, respectively. Additionally, the dust storms accelerated snow aging,
710 as indicated by the growth of R_{eff}. Furthermore, the dust plumes from the Taklamakan
711 Desert traveled eastward, depositing dust across much of the snow-covered area (>630
712 km²) in the Qilian Mountains, where the dust content significantly increased to 194–

713 360 $\mu\text{g g}^{-1}$, causing a considerable increase in snow albedo reduction (radiative forcing)
714 of 0.092–0.153 (22–38 W m^{-2}). The spatial distribution of the snow-darkening effect
715 varied across all three mountain ranges due to the uneven deposition of dust, with the
716 most significant snow darkening observed in the high elevation range of 4000–5500 m.
717 Moreover, by comparing our satellite-derived results with previous field measurements,
718 we found that severe dust storms, occurring over short periods, have a more profound
719 effect on snow darkening compared with the relatively slow deposition of dust in the
720 absence of dust storms. These severe snow darkening events were not limited to the
721 three typical cases but occurred widely (Figures S13-S21). This highlights the
722 importance of satellite-derived analyses in capturing extreme dust deposition events
723 that may be challenging to detect through field measurements and climate model
724 simulations. Our findings underscore the significance of understanding the impact of
725 dust deposition on snow albedo and radiative forcing for accurate assessment of the
726 environmental effects of these extreme events.

727 ~~The Taklamakan Desert, the second largest shifting sand desert on Earth, annually~~
728 ~~emits vast amounts of dust into the atmosphere that eventually settles onto the~~
729 ~~snowpack across the surrounding high mountains. We combined MODIS satellite data~~
730 ~~analysis and SNICAR model simulations to reveal significant snow-darkening events~~
731 ~~and quantify the snow albedo reduction and radiative forcing caused by severe dust~~
732 ~~storms.~~

733 ~~The satellite observations captured significant snow darkening over the 3000–6000 m~~
734 ~~elevation range across the Tien Shan and Kunlun Mountains, which could be attributed~~
735 ~~to the high uplift of dust owing to the local topography and atmospheric circulation.~~
736 ~~The impacted area spanned the track of the dust storm and impacted almost all of the~~
737 ~~snow-covered areas across the Tien Shan ($>2100 \text{ km}^2$) and Kunlun Mountains (>600~~
738 ~~km^2), including the summits. The dust content in the snowpack increased to 42–192~~
739 ~~and 170–360 $\mu\text{g g}^{-1}$, with significant increases in snow albedo reduction (radiative~~
740 ~~forcing) of 0.028–0.079 (11–31.5 W m^{-2}) and 0.088–0.136 (31–49 W m^{-2}) across the~~
741 ~~Tien Shan and Kunlun Mountains, respectively. Furthermore, these dust events~~
742 ~~accelerated snow aging, as indicated by the R_{eff} growth. The dust plumes from the~~

743 Taklamakan Desert also traveled to the east, almost 1000 km from the Tarim Basin,
744 and deposited dust across much of the snow-covered area ($>630 \text{ km}^2$) in the Qilian
745 Mountains. This dust deposition significantly increased the dust content to $194\text{--}360 \mu\text{g}$
746 g^{-1} , causing a considerable increase in snow albedo reduction (radiative forcing) of
747 $0.092\text{--}0.153$ ($22\text{--}38 \text{ W m}^{-2}$). The spatial distribution of the snow-darkening effect
748 varied across all three mountain ranges owing to the uneven deposition of dust.
749 Furthermore, the most significant snow-darkening was observed in the high-elevation
750 range (4000–5500 m). We also compared our satellite-derived results with previous
751 field measurements. Our results indicate that severe dust storms, which occur over short
752 periods, have a more profound effect on snow-darkening compared with the relatively
753 slow deposition of dust when there are no dust storms. We therefore demonstrate that
754 satellite-derived analyses of dust deposition and its impact on snow albedo and radiative
755 forcing are crucial for rapidly and accurately capturing extreme dust deposition events
756 that may be difficult to detect through field measurements and climate model
757 simulations.

758

759

760

761

762

763

764

765

766

767

768

769

770

771 *Data availability.* All datasets and codes used to produce this study can be obtained by
772 contacting Wei Pu (puwei@lzu.edu.cn).

773 *Author contributions.* WP and XW designed the study and developed the overarching
774 research goals and aims. YX carried the study out and wrote the first draft with
775 contributions from all co-authors. YX processed the data with the assistance of YC, SY,
776 TS, XC, XN, DW, ~~and~~ JC and YZ. WP and XW assumed oversight and leadership
777 responsibility for the research activity planning and execution. All authors contributed
778 to the improvement of results and revised the final paper.

779 *Competing interests.* The authors declare that they have no conflict of interest.

780 *Acknowledgements.* The Lanzhou University group acknowledges support from the
781 National Science Fund for Distinguished Young Scholars, the State Key Laboratory of
782 Cryosphere Science Open Fund and the National Natural Science Foundation of China.
783 We appreciate Dr. Boyuan Zhang's assistance with the code improvements. We thank
784 Lanzhou City's scientific research funding subsidy to Lanzhou University and the
785 Supercomputing Center of Lanzhou University for providing the computing services.

786 *Financial support.* This research was supported by the National Science Fund for
787 Distinguished Young Scholars (42025102), the State Key Laboratory of Cryosphere
788 Science Open Fund (SKLCS-OP-2021-05) and the National Natural Science
789 Foundation of China ([42375068](#) and [42075061](#)) and the Natural Science Foundation of
790 Gansu province, China (21ZDKA0017). -

791 **Reference**

792 [Arun, B. S., Aswini, A. R., Gogoi, M. M., Hegde, P., Kumar Kompalli, S., Sharma, P.,](#)
793 [and Suresh Babu, S.: Physico-chemical and optical properties of aerosols at a](#)
794 [background site \(~4 km a.s.l.\) in the western Himalayas, Atmospheric](#)
795 [Environment, 218, 10.1016/j.atmosenv.2019.117017, 2019.](#)

796 [Arun, B. S., Gogoi, M. M., Borgohain, A., Hegde, P., Kundu, S. S., and Babu, S. S.:](#)
797 [Role of sulphate and carbonaceous aerosols on the radiative effects of aerosols](#)
798 [over a remote high-altitude site Lachung in the Eastern Himalayas, Atmospheric](#)
799 [Research, 263, 10.1016/j.atmosres.2021.105799, 2021a.](#)

800 [Arun, B. S., Gogoi, M. M., Hegde, P., Borgohain, A., Boreddy, S. K. R., Kundu, S. S.,](#)
801 [and Babu, S. S.: Carbonaceous Aerosols over Lachung in the Eastern Himalayas:](#)
802 [Primary Sources and Secondary Formation of Organic Aerosols in a Remote High-](#)
803 [Altitude Environment, ACS Earth and Space Chemistry, 5, 2493-2506,](#)
804 [10.1021/acsearthspacechem.1c00190, 2021b.](#)

805 Bair, E. H., Stillinger, T., and Dozier, J.: Snow property inversion from remote sensing
806 (SPIReS): A generalized multispectral unmixing approach with examples from
807 MODIS and Landsat 8 OLI, IEEE Transactions on Geoscience and Remote
808 Sensing, 59, 7270-7284, 10.1109/tgrs.2020.3040328, 2020.

809 Baladima, F., Thomas, J. L., Voisin, D., Dumont, M., Junquas, C., Kumar, R., Lavaysse,
810 C., Marelle, L., Parrington, M., and Flemming, J.: Modeling an extreme dust
811 deposition event to the French Alpine seasonal snowpack in April 2018:
812 Meteorological context and predictions of dust deposition, Journal of Geophysical
813 Research: Atmospheres, 127, 10.1029/2021jd035745, 2022.

814 Bormann, K. J., Brown, R. D., Derksen, C., Painter, T. H.: Estimating snow-cover
815 trends from space, Nature Climate Change, 11, 924-928, 10.1038/s41558-018-
816 0318-3, 2018.

817 [Chaubey, J. P., Moorthy, K. K., Babu, S. S., Nair, V. S., and Tiwari, A.: Black carbon](#)
818 [aerosols over coastal Antarctica and its scavenging by snow during the Southern](#)
819 [Hemispheric summer, Journal of Geophysical Research: Atmospheres, 115,](#)
820 [10.1029/2009jd013381, 2010.](#)

821 Chen, B., Song, Z., Huang, J., Zhang, P., Hu, X., Zhang, X., Guan, X., Ge, J., and Zhou,
822 X.: Estimation of atmospheric PM10 Concentration in China using an
823 interpretable deep learning model and top-of-the-atmosphere reflectance data from
824 China's new generation geostationary meteorological satellite, FY-4A, Journal of
825 Geophysical Research: Atmospheres, 127, 10.1029/2021jd036393, 2022.

826 Chen, S., Huang, J., Zhao, C., Qian, Y., Leung, L. R., and Yang, B.: Modeling the
827 transport and radiative forcing of Taklimakan dust over the Tibetan Plateau: A case
828 study in the summer of 2006, Journal of Geophysical Research: Atmospheres, 118,
829 797-812, 10.1002/jgrd.50122, 2013.

830 Chen, S., Huang, J., Li, J., Jia, R., Jiang, N., Kang, L., Ma, X., and Xie, T.: Comparison
831 of dust emissions, transport, and deposition between the Taklimakan Desert and
832 Gobi Desert from 2007 to 2011, Science China Earth Sciences, 60, 1338-1355,
833 10.1007/s11430-016-9051-0, 2017a.

834 Chen, S., Huang, J., Kang, L., Wang, H., Ma, X., He, Y., Yuan, T., Yang, B., Huang, Z.,

835 and Zhang, G.: Emission, transport, and radiative effects of mineral dust from the
836 Taklimakan and Gobi deserts: comparison of measurements and model results,
837 Atmospheric Chemistry and Physics, 17, 2401-2421, 10.5194/acp-17-2401-2017,
838 2017b.

839 Chen, W., Wang, X., Cui, J., Cao, X., Pu, W., Zheng, X., Ran, H., and Ding, J.: Radiative
840 forcing of black carbon in seasonal snow of wintertime based on remote sensing
841 over Xinjiang, China, Atmospheric Environment, 247,
842 10.1016/j.atmosenv.2021.118204, 2021.

843 Clow, D. W., Williams, M. W., and Schuster, P. F.: Increasing aeolian dust deposition to
844 snowpacks in the Rocky Mountains inferred from snowpack, wet deposition, and
845 aerosol chemistry, Atmospheric Environment, 146, 183-194,
846 10.1016/j.atmosenv.2016.06.076, 2016.

847 Cohen, J. and Rind, D.: The Effect of Snow Cover on the Climate, J. Climate, 4, 689–
848 706, 10.1175/1520-0442(1991)004<0689:Teosco>2.0.Co;2, 1991.

849 Copernicus Climate Change Service: ERA5: Fifth generation of ECMWF atmospheric
850 reanalysis of the global climate, Copernicus Climate Change Service Climate Data
851 Store (CDS), 2017.

852 Cordero, R., Sepúlveda, E., Feron, S., Damiani, A., Fernandez, F., Neshyba, S., Rowe,
853 P. M., Asencio, V., Carrasco, J., Alfonso, J. A., Llanillo, P., Wachter, P., Seckmeyer,
854 G., Stepanova, M., Carrera, J. M., Jorquera, J., Wang, C., Malhotra, A., Dana, J.,
855 Khan, A. L., and Casassa, G.: Black carbon footprint of human presence in
856 Antarctica, Nature Communications, 13, 2041-1723, s41467-022-28560-w, 2022.

857 Cui, J., Shi, T., Zhou, Y., Wu, D., Wang, X., and Pu, W.: Satellite-based radiative forcing
858 by light-absorbing particles in snow across the Northern Hemisphere,
859 Atmospheric Chemistry and Physics, 21, 269-288, 10.5194/acp-21-269-2021,
860 2021.

861 Dang, C., Warren, S. G., Fu, Q., Doherty, S. J., Sturm, M., and Su, J.: Measurements of
862 light-absorbing particles in snow across the Arctic, North America, and China:
863 Effects on surface albedo, Journal of Geophysical Research: Atmospheres, 122,
864 10.1002/2017jd027070, 2017.

865 Di Mauro, B., Fava, F., Ferrero, L., Garzonio, R., Baccolo, G., Delmonte, B., and
866 Colombo, R.: Mineral dust impact on snow radiative properties in the European
867 Alps combining ground, UAV, and satellite observations, Journal of Geophysical
868 Research: Atmospheres, 120, 6080-6097, 10.1002/2015jd023287, 2015.

869 Dong, Z., Li, Z., Wang, F., and Zhang, M.: Characteristics of atmospheric dust
870 deposition in snow on the glaciers of the eastern Tien Shan, China, Journal of
871 Glaciology, 55, 797-804, 10.3189/002214309790152393, 2009.

872 Dong, Z., Qin, D., Chen, J., Qin, X., Ren, J., Cui, X., Du, Z., and Kang, S.:
873 Physicochemical impacts of dust particles on alpine glacier meltwater at the
874 Laohugou Glacier basin in western Qilian Mountains, China, Science of the Total
875 Environment, 493, 930-942, 10.1016/j.scitotenv.2014.06.025, 2014.

876 Dong, Z., Brahney, J., Kang, S., Elser, J., Wei, T., Jiao, X., and Shao, Y.: Aeolian dust
877 transport, cycle and influences in high-elevation cryosphere of the Tibetan Plateau
878 region: New evidences from alpine snow and ice, Earth-Science Reviews, 211,

879 10.1016/j.earscirev.2020.103408, 2020.

880 Dong, Q., Huang, Z., Li, W., Li, Z., Song, X., Liu, W., Wang, T., Bi, J., and Shi, J.:

881 Polarization lidar measurements of dust optical properties at the junction of the

882 Taklimakan Desert–Tibetan Plateau, *Remote Sensing*, 14, 10.3390/rs14030558,

883 2022.

884 Dumont, M., Brun, E., Picard, G., Michou, M., Libois, Q., Petit, J. R., Geyer, M., Morin,

885 S., and Josse, B.: Contribution of light-absorbing impurities in snow to

886 Greenland’s darkening since 2009, *Nature Geoscience*, 7, 509-512,

887 10.1038/ngeo2180, 2014.

888 Dumont, M., Tuzet, F., Gascoïn, S., Picard, G., Kutuzov, S., Lafaysse, M., Cluzet, B.,

889 Nheili, R., and Painter, T. H.: Accelerated snow melt in the Russian Caucasus

890 Mountains after the Saharan dust outbreak in March 2018, *Journal of Geophysical*

891 *Research: Earth Surface*, 125, 10.1029/2020jf005641, 2020.

892 Flanner, M. G., Zender, C. S., Randerson, J. T., and Rasch, P. J.: Present-day climate

893 forcing and response from black carbon in snow, *Journal of Geophysical Research*,

894 112, 10.1029/2006jd008003, 2007.

895 Flanner, M. G., Zender, C. S., Hess, P. G., Mahowald, N. M., Painter, T. H., Ramanathan,

896 V., and Rasch, P. J.: Springtime warming and reduced snow cover from

897 carbonaceous particles, *Atmospheric Chemistry and Physics*, 9, 2481–2497,

898 10.5194/acp-9-2481-2009, 2009.

899 Flanner, M. G., Arnheim, J. B., Cook, J. M., Dang, C., He, C., Huang, X., Singh, D.,

900 Skiles, S. M., Whicker, C. A., and Zender, C. S.: SNICAR-ADv3: a community

901 tool for modeling spectral snow albedo, *Geoscientific Model Development*, 14,

902 7673-7704, 10.5194/gmd-14-7673-2021, 2021.

903 Gautam, R., Hsu, N. C., Lau, W. K. M., and Yasunari, T. J.: Satellite observations of

904 desert dust-induced Himalayan snow darkening, *Geophysical Research Letters*, 40,

905 988-993, 10.1002/grl.50226, 2013.

906 Ge, J. M., Huang, J. P., Xu, C. P., Qi, Y. L., and Liu, H. Y.: Characteristics of Taklimakan

907 dust emission and distribution: A satellite and reanalysis field perspective, *Journal*

908 *of Geophysical Research: Atmospheres*, 119, 11,772-711,783,

909 10.1002/2014jd022280, 2014.

910 [Gogoi, M. M., Babu, S. S., Pandey, S. K., Nair, V. S., Vaishya, A., Girach, I. A., and](#)

911 [Koushik, N.: Scavenging ratio of black carbon in the Arctic and the Antarctic,](#)

912 [Polar Science](#), 16, 10-22, 10.1016/j.polar.2018.03.002, 2018.

913 [Gogoi M. M., Babu, S. S., Arun, B. S., Moorthy, K. K., Ajay, A., Ajay, P., Suryavanshi,](#)

914 [A., Borgohain, A., Guha, A., Shaikh, A., Pathak, B., Gharai, B., Ramasamy, B.,](#)

915 [Balakrishnaiah, G., Menon, H. B., Kuniyal, J. C., Krishnan, J., Gopal, K. R.,](#)

916 [Maheswari, M., Naja, M., Kaur, P., Bhuyan, P. K., Gupta, P., Singh, P., Srivastava,](#)

917 [P., Singh, R. S., Kumar, R., Rastogi, S., Kundu, S. S., Kompalli, S. K., Panda, S.,](#)

918 [Rao, T. C., Das, T., and Kant, Y.: Response of ambient BC concentration across](#)

919 [the Indian region to the nation-wide lockdown: results from the ARFINET](#)

920 [measurements of ISRO-GBP](#), *Current Science*, 120, 10.18520/cs/v120/i2/341-351,

921 [2021a.](#)

922 [Gogoi, M. M., Pandey, S. K., Arun, B. S., Nair, V. S., Thakur, R. C., Chaubey, J. P.,](#)

923 [Tiwari, A., Manoj, M. R., Kompalli, S. K., Vaishya, A., Prijith, S. S., Hegde, P.,](#)
924 [and Babu, S. S.: Long-term changes in aerosol radiative properties over Ny-](#)
925 [Ålesund: Results from Indian scientific expeditions to the Arctic, *Polar Science*,](#)
926 [30, 10.1016/j.polar.2021.100700, 2021b.](#)

927 Gui, K., Yao, W., Che, H., An, L., Zheng, Y., Li, L., Zhao, H., Zhang, L., Zhong, J.,
928 Wang, Y., and Zhang, X.: Record-breaking dust loading during two mega dust
929 storm events over northern China in March 2021: aerosol optical and radiative
930 properties and meteorological drivers, *Atmospheric Chemistry and Physics*, 22,
931 7905-7932, 10.5194/acp-22-7905-2022, 2022.

932 Hadley, O. L. and Kirchstetter, T. W.: Black-carbon reduction of snow albedo, *Nat. Clim.*
933 *Change*, 2, 437–440, 10.1038/nclimate1433, 2012.

934 Han, Y., Wang, T., Tang, J., Wang, C., Jian, B., Huang, Z., and Huang, J.: New insights
935 into the Asian dust cycle derived from CALIPSO lidar measurements, *Remote*
936 *Sensing of Environment*, 272, 10.1016/j.rse.2022.112906, 2022.

937 He, C., Takano, Y., Liou, K.-N., Yang, P., Li, Q., and Chen, F.: Impact of snow grain
938 shape and black carbon–snow internal mixing on snow optical properties:
939 Parameterizations for climate models, *Journal of Climate*, 30, 10019-10036,
940 10.1175/jcli-d-17-0300.1, 2017.

941 He, C., Liou, K. N., Takano, Y., Yang, P., Qi, L., and Chen, F.: Impact of grain shape
942 and multiple black carbon internal mixing on snow albedo: Parameterization and
943 radiative effect analysis, *Journal of Geophysical Research: Atmospheres*, 123,
944 1253-1268, 10.1002/2017jd027752, 2018.

945 Huang, H., Qian, Y., He, C., Bair, E. H., and Rittger, K.: Snow albedo feedbacks
946 enhance snow impurity-induced radiative forcing in the Sierra Nevada,
947 *Geophysical Research Letters*, 49, e2022GL098102, 10.1029/2022GL098102,
948 2022.

949 Huang, J., Minnis, P., Yi, Y., Tang, Q., Wang, X., Hu, Y., Liu, Z., Ayers, K., Trepte, C.,
950 and Winker, D.: Summer dust aerosols detected from CALIPSO over the Tibetan
951 Plateau, *Geophysical Research Letters*, 34, 10.1029/2007gl029938, 2007.

952 Huang, J., Minnis, P., Chen, B., Huang, Z., Liu, Z., Zhao, Q., Yi, Y., and Ayers, J. K.:
953 Long-range transport and vertical structure of Asian dust from CALIPSO and
954 surface measurements during PACDEX, *Journal of Geophysical Research*, 113,
955 10.1029/2008jd010620, 2008.

956 Huang, J., Wang, T., Wang, W., Li, Z., and Yan, H.: Climate effects of dust aerosols
957 over East Asian arid and semiarid regions, *Journal of Geophysical Research:*
958 *Atmospheres*, 119, 10.1002/2014jd021796, 2014.

959 Immerzeel, W. W. and Bierkens, M. F. P.: Asia's water balance, *Nature Geoscience*, 5,
960 841-842, 10.1038/ngeo1643, 2012.

961 Jia, R., Liu, Y., Chen, B., Zhang, Z., and Huang, J.: Source and transportation of summer
962 dust over the Tibetan Plateau, *Atmospheric Environment*, 123, 210-219,
963 10.1016/j.atmosenv.2015.10.038, 2015.

964 Kang, L., Huang, J., Chen, S., and Wang, X.: Long-term trends of dust events over
965 Tibetan Plateau during 1961–2010, *Atmospheric Environment*, 125, 188-198,
966 10.1016/j.atmosenv.2015.10.085, 2016.

967 Kraaijenbrink, P. D. A., Bierkens, M. F. P., Lutz, A. F., and Immerzeel, W. W.: Impact
968 of a global temperature rise of 1.5 degrees Celsius on Asia's glaciers, *Nature*, 549,
969 257-260, 10.1038/nature23878, 2017.

970 Kraaijenbrink, P. D. A., Stigter, E. E., Yao, T., and Immerzeel, W. W.: Climate change
971 decisive for Asia's snow meltwater supply, *Nature Climate Change*, 11, 591-597,
972 10.1038/s41558-021-01074-x, 2021.

973 Li, Y., Chen, Y., and Li, Z.: Climate and topographic controls on snow phenology
974 dynamics in the Tianshan Mountains, Central Asia, *Atmospheric Research*, 236,
975 10.1016/j.atmosres.2019.104813, 2020.

976 Li, Y., Kang, S., Zhang, X., Chen, J., Schmale, J., Li, X., Zhang, Y., Niu, H., Li, Z., Qin,
977 X., He, X., Yang, W., Zhang, G., Wang, S., Shao, L., and Tian, L.: Black carbon
978 and dust in the Third Pole glaciers: Revaluated concentrations, mass absorption
979 cross-sections and contributions to glacier ablation, *Science of the Total
980 Environment*, 789, 147746, 10.1016/j.scitotenv.2021.147746, 2021.

981 Li, Y., Kang, S., Zhang, X., Li, C., Chen, J., Qin, X., Shao, L., and Tian, L.: Dust
982 dominates the summer melting of glacier ablation zones on the northeastern
983 Tibetan Plateau, *Science of the Total Environment*, 856, 159214,
984 10.1016/j.scitotenv.2022.159214, 2022.

985 Liang, P., Chen, B., Yang, X., Liu, Q., Li, A., Mackenzie, L., and Zhang, D.: Revealing
986 the dust transport processes of the 2021 mega dust storm event in northern China,
987 *Science Bulletin*, 67, 21-24, 10.1016/j.scib.2021.08.014, 2021.

988 Ménégoz, M., Krinner, G., Balkanski, Y., Boucher, O., Cozic, A., Lim, S., Ginot, P., Laj,
989 P., Gallée, H., Wagnon, P., Marinoni, A., and Jacobi, H. W.: Snow cover sensitivity
990 to black carbon deposition in the Himalayas: from atmospheric and ice core
991 measurements to regional climate simulations, *Atmospheric Chemistry and
992 Physics*, 14, 4237-4249, 10.5194/acp-14-4237-2014, 2014.

993 Meng, L., Yang, X., Zhao, T., He, Q., Lu, H., Mamtimin, A., Huo, W., Yang, F., and Liu,
994 C.: Modeling study on three-dimensional distribution of dust aerosols during a
995 dust storm over the Tarim Basin, Northwest China, *Atmospheric Research*, 218,
996 285-295, 10.1016/j.atmosres.2018.12.006, 2018.

997 Ming, J., Xiao, C. D., Wang, F. T., Li, Z. Q., and Li, Y. M.: Grey Tianshan Urumqi
998 Glacier No.1 and light-absorbing impurities, *Environmental Science and Pollution
999 Research*, 23, 9549-9558, 10.1007/s11356-016-6182-7, 2016.

1000 Mishra, S. K., Hayse, J., Veselka, T., Yan, E., Kayastha, R. B., LaGory, K., McDonald,
1001 K., and Steiner, N.: An integrated assessment approach for estimating the
1002 economic impacts of climate change on River systems: An application to
1003 hydropower and fisheries in a Himalayan River, Trishuli, *Environmental Science
1004 & Policy*, 87, 102-111, 10.1016/j.envsci.2018.05.006, 2018.

1005 Mishra, S. K., Rupper, S., Kapnick, S., Casey, K., Chan, H. G., Ciraci, E., Haritashya,
1006 U., Hayse, J., Kargel, J. S., Kayastha, R. B., Krakauer, N. Y., Kumar, S. V.,
1007 Lammers, R. B., Maggioni, V., Margulis, S. A., Olson, M., Osmanoglu, B., Qian,
1008 Y., McLarty, S., Rittger, K., Rounce, D. R., Shean, D., Velicogna, I., Veselka, T.
1009 D., and Arendt, A.: Grand challenges of hydrologic modeling for food-energy-
1010 water nexus security in High Mountain Asia, *Frontiers in Water*, 3,

1011 10.3389/frwa.2021.728156, 2021.

1012 Negi, H. S. and Kokhanovsky, A.: Retrieval of snow grain size and albedo of western
1013 Himalayan snow cover using satellite data, *The Cryosphere*, 5, 831-847,
1014 10.5194/tc-5-831-2011, 2011.

1015 Notarnicola, C.: Hotspots of snow cover changes in global mountain regions over
1016 2000–2018, *Remote Sensing of Environment.*, 243, 111781,
1017 10.1016/j.rse.2020.111781, 2020.

1018 Niu, X., Pu, W., Fu, P., Chen, Y., Xing, Y., Wu, D., Chen, Z., Shi, T., Zhou, Y., Wen, H.,
1019 and Wang, X.: Fluorescence characteristics, absorption properties, and radiative
1020 effects of water-soluble organic carbon in seasonal snow across northeastern China,
1021 *Atmospheric Chemistry and Physics*, 22, 14075-14094, 10.5194/acp-22-14075-
1022 2022, 2022.

1023 Okada, K., Kai, K.: Atmospheric mineral particles collected at Qira in the Taklamakan
1024 Desert, China, *Atmospheric Environment*, 38, 6927-6935,
1025 10.1016/j.atmosenv.2004.03.078, 2004.

1026 Orsolini, Y., Wegmann, M., Dutra, E., Liu, B., Balsamo, G., Yang, K., de Rosnay, P.,
1027 Zhu, C., Wang, W., Senan, R., and Arduini, G.: Evaluation of snow depth and snow
1028 cover over the Tibetan Plateau in global reanalyses using in situ and satellite
1029 remote sensing observations, *The Cryosphere*, 13, 2221-2239, 10.5194/tc-13-
1030 2221-2019, 2019.

1031 Painter, T. H., Rittger, K., McKenzie, C., Slaughter, P., Davis, R. E., and Dozier, J.:
1032 Retrieval of subpixel snow covered area, grain size, and albedo from MODIS,
1033 *Remote Sensing of Environment*, 113, 868-879, 10.1016/j.rse.2009.01.001, 2009.

1034 Painter, T. H., Bryant, A. C., and Skiles, S. M.: Radiative forcing by light absorbing
1035 impurities in snow from MODIS surface reflectance data, *Geophysical Research*
1036 *Letters*, 39, n/a-n/a, 10.1029/2012gl052457, 2012.

1037 Painter, T. H., Skiles, S. M., Deems, J. S., Brandt, W. T., and Dozier, J.: Variation in
1038 rising limb of colorado river snowmelt runoff hydrograph controlled by dust
1039 radiative forcing in snow, *Geophysical Research Letters*, 45, 797-808,
1040 10.1002/2017gl075826, 2017.

1041 Patterson, E.M.: Optical properties of the crustal aerosol: Relation to chemical and
1042 physical characteristics, *Journal of Geophysical Research: Atmospheres*, 86, 3236-
1043 3246, 10.1029/JC086iC04p03236, 1981.

1044 Pu, W., Cui, J., Shi, T., Zhang, X., He, C., and Wang, X.: The remote sensing of radiative
1045 forcing by light-absorbing particles (LAPs) in seasonal snow over northeastern
1046 China, *Atmospheric Chemistry and Physics*, 19, 9949-9968, 10.5194/acp-19-
1047 9949-2019, 2019.

1048 Pu, W., Cui, J., Wu, D., Shi, T., Chen, Y., Xing, Y., Zhou, Y., and Wang, X.:
1049 Unprecedented snow darkening and melting in New Zealand due to 2019–2020
1050 Australian wildfires, *Fundamental Research*, 1, 224-231,
1051 10.1016/j.fmre.2021.04.001, 2021.

1052 Pulliainen, J., Luojus, K., Derksen, C., Mudryk, L., Lemmetyinen, J., Salminen, M.,
1053 Ikonen, J., Takala, M., Cohen, J., Smolander, T., and Norberg, J.: Patterns and
1054 trends of Northern Hemisphere snow mass from 1980 to 2018, 581, 294-298,

1055 s41586-020-2258-0, 2020.

1056 Qian, Y., Yasunari, T. J., Doherty, S. J., Flanner, M. G., Lau, W. K. M., Ming, J., Wang,
1057 H., Wang, M., Warren, S. G., and Zhang, R.: Light-absorbing particles in snow and
1058 ice: Measurement and modeling of climatic and hydrological impact, *Advances in*
1059 *Atmospheric Sciences*, 32, 64-91, 10.1007/s00376-014-0010-0, 2015.

1060 Qiu, X., Zeng, Y., and Miao, Q.: Sand-dust storms in China: temporal-spatial
1061 distribution and tracks of source lands, *Journal of Geographical Sciences*. 11, 253–
1062 260, 10.1007/BF02892308, 2001.

1063 Reveillet, M., Dumont, M., Gascoïn, S., Lafaysse, M., Nabat, P., Ribes, A., Nheili, R.,
1064 Tuzet, F., Menegoz, M., Morin, S., Picard, G., and Ginoux, P.: Black carbon and
1065 dust alter the response of mountain snow cover under climate change, *Nature*
1066 *Communication*, 13, 5279, 10.1038/s41467-022-32501-y, 2022.

1067 Ricchiazzi, P., Yang, S. R., Gautier, C., and Sowle, D.: SBDART: A research and
1068 teaching software tool for plane-parallel radiative transfer in the Earth's
1069 atmosphere, *Bulletin of the American Meteorological Society.*, 79, 2101–2114,
1070 10.1175/1520-0477(1998)079<2101:Sarats>2.0.Co;2, 1998.

1071 Rittger, K., Painter, T. H., and Dozier, J.: Assessment of methods for mapping snow
1072 cover from MODIS, *Advances in Water Resources*, 51, 367-380,
1073 10.1016/j.advwatres.2012.03.002, 2013.

1074 [Rohde, A., Vogel, H., Hoshyaripour, H. A., Kottmeier C., and Vogel, B.: Regional](#)
1075 [Impact of Snow-Darkening on Snow Pack and the Atmosphere During a Severe](#)
1076 [Saharan Dust Deposition Event in Eurasia, *Journal of Geophysical Research:*](#)
1077 [Earth Surface](#), 128, 10.1029/2022JF007016, 2023.

1078 Roychoudhury, C., He, C., Kumar, R., McKinnon, J. M., and Arellano, A. F.: On the
1079 relevance of aerosols to snow cover variability over High Mountain Asia,
1080 *Geophysical Research Letters*, 49, 10.1029/2022gl099317, 2022.

1081 Sang, J., Kim, M.-K., Lau, W. K. M., and Kim, K.-M.: Possible Impacts of snow
1082 darkening effects on the hydrological cycle over western Eurasia and east Asia,
1083 *Atmosphere*, 10, 10.3390/atmos10090500, 2019.

1084 Sarangi, C., Qian, Y., Rittger, K., Bormann, K. J., Liu, Y., Wang, H., Wan, H., Lin, G.,
1085 and Painter, T. H.: Impact of light-absorbing particles on snow albedo darkening
1086 and associated radiative forcing over high-mountain Asia: high-resolution WRF-
1087 Chem modeling and new satellite observations, *Atmospheric Chemistry and*
1088 *Physics*, 19, 7105-7128, 10.5194/acp-19-7105-2019, 2019.

1089 Sarangi, C., Qian, Y., Rittger, K., Ruby Leung, L., Chand, D., Bormann, K. J., and
1090 Painter, T. H.: Dust dominates high-altitude snow darkening and melt over high-
1091 mountain Asia, *Nature Climate Change*, 10, 1045-1051, 10.1038/s41558-020-
1092 00909-3, 2020.

1093 Schmale, J., Flanner, M., Kang, S. C., Sprenger, M., Zhang, Q. G., Guo, J. M., Li, Y.,
1094 Schwikowski, M., and Farinotti, D.: Modulation of snow reflectance and
1095 snowmelt from Central Asian glaciers by anthropogenic black carbon, *Scientific*
1096 *Reports*, 7, 40501, 10.1038/srep40501, 2017.

1097 Siegmund., A. and Menz., G.: Fernes nah gebracht – satelliten- und luftbildeinsatz zur
1098 analyse von umweltveränderungen im geographieunterricht, *Geographie und*

1099 Schule, 154, 2–10, 2005.

1100 Shao, Y. and Dong, C. H.: A review on East Asian dust storm climate, modelling and
1101 monitoring, *Global and Planetary Change*, 52, 1–22,
1102 10.1016/j.gloplacha.2006.02.011, 2006.

1103 She, J., Zhang, Y., Li, X., and Feng, X.: Spatial and temporal characteristics of snow
1104 cover in the Tizinafu watershed of the Western Kunlun Mountains, *Remote
1105 Sensing*, 7, 3426–3445, 10.3390/rs70403426, 2015.

1106 Shi, T., Pu, W., Zhou, Y., Cui, J., Zhang, D., and Wang, X.: Albedo of black carbon-
1107 contaminated snow across Northwestern China and the validation with model
1108 simulation, *Journal of Geophysical Research: Atmospheres*, 125,
1109 10.1029/2019jd032065, 2020.

1110 Shi, T., Cui, J., Chen, Y., Zhou, Y., Pu, W., Xu, X., Chen, Q., Zhang, X., and Wang, X.:
1111 Enhanced light absorption and reduced snow albedo due to internally mixed
1112 mineral dust in grains of snow, *Atmospheric Chemistry and Physics*, 21, 6035–
1113 6051, 10.5194/acp-21-6035-2021, 2021.

1114 Shi, T., Cui, J., Wu, D., Xing, Y., Chen, Y., Zhou, Y., Pu, W., and Wang, X.: Snow albedo
1115 reductions induced by the internal/external mixing of black carbon and mineral
1116 dust, and different snow grain shapes across northern China, *Environmental
1117 Research*, 208, 112670, 10.1016/j.envres.2021.112670, 2022a.

1118 Shi, T., Chen, Y., Xing, Y., Niu, X., Wu, D., Cui, J., Zhou, Y., Pu, W., and Wang, X.:
1119 Assessment of the combined radiative effects of black carbon in the atmosphere
1120 and snowpack in the Northern Hemisphere constrained by surface observations,
1121 *Environmental Science: Atmospheres*, 2, 702–713, 10.1039/d2ea00005a, 2022b.

1122 Shi, Z., Xie, X., Li, X., Yang, L., Xie, X., Lei, J., Sha, Y., and Liu, X.: Snow-darkening
1123 versus direct radiative effects of mineral dust aerosol on the Indian summer
1124 monsoon onset: role of temperature change over dust sources, *Atmospheric
1125 Chemistry and Physics*, 19, 1605–1622, 10.5194/acp-19-1605-2019, 2019.

1126 Skiles, S. M. and Painter, T.: Daily evolution in dust and black carbon content, snow
1127 grain size, and snow albedo during snowmelt, Rocky Mountains, Colorado,
1128 *Journal of Glaciology*, 63, 118–132, 10.1017/jog.2016.125, 2016.

1129 Skiles, S. M., Flanner, M., Cook, J. M., Dumont, M., and Painter, T. H.: Radiative
1130 forcing by light-absorbing particles in snow, *Nature Climate Change*, 8, 964–971,
1131 10.1038/s41558-018-0296-5, 2018a.

1132 Skiles, S. M., Mallia, D. V., Hallar, A. G., Lin, J. C., Lambert, A., Petersen, R., and
1133 Clark, S.: Implications of a shrinking Great Salt Lake for dust on snow deposition
1134 in the Wasatch Mountains, UT, as informed by a source to sink case study from
1135 the 13–14 April 2017 dust event, *Environmental Research Letters*, 13,
1136 10.1088/1748-9326/aaefd8, 2018b.

1137 Sun, J., Zhang, M., and Liu, T.: Spatial and temporal characteristics of dust storms in
1138 China and its surrounding regions, 1960–1999: Relations to source area and
1139 climate, *Journal of Geophysical Research: Atmospheres*, 106, 10325–10333,
1140 10.1029/2000jd900665, 2001.

1141 Tang, W., Dai, T., Cheng, Y., Wang, S., and Liu, Y.: A study of a severe spring dust event
1142 in 2021 over east Asia with WRF-Chem and multiple platforms of observations,

1143 Remote Sensing, 14, 10.3390/rs14153795, 2022.

1144 Teillet, P. M., Guindon, B., and Goodenough, D. G.: On the slope-aspect correction of
1145 multispectral scanner data, Canadian Journal of Remote Sensing, 8, 84-106,
1146 10.1080/07038992.1982.10855028, 1982.

1147 [Thakur, R. C., Arun, B. S., Gogoi, M. M., Thamban, M., Thayyen, R. J., Redkar, B. L.,
1148 and Suresh Babu, S.: Multi-layer distribution of Black Carbon and inorganic ions
1149 in the snowpacks of western Himalayas and snow albedo forcing, Atmospheric
1150 Environment, 261, 10.1016/j.atmosenv.2021.118564, 2021.](#)

1151 Usha, K. H., Nair, V. S., and Babu, S. S.: Deciphering the role of aerosol-induced snow
1152 albedo feedback on dust emission over the Tibetan Plateau, Journal of Geophysical
1153 Research: Atmospheres, 127, 10.1029/2021jd036384, 2022.

1154 Wake, C. P., Mayewski, P. A., Li, Z., Han, J., and Qin, D.: Modern eolian dust deposition
1155 in central Asia, Tellus B: Chemical and Physical Meteorology, 46,
1156 10.3402/tellusb.v46i3.15793, 1994.

1157 Wang, X., Huang, J., Ji, M., and Higuchi, K.: Variability of East Asia dust events and
1158 their long-term trend, Atmospheric Environment, 42, 3156-3165,
1159 10.1016/j.atmosenv.2007.07.046, 2008.

1160 Wang, X., Doherty, S. J., and Huang, J.: Black carbon and other light-absorbing
1161 impurities in snow across Northern China, Journal of Geophysical Research:
1162 Atmospheres, 118, 1471-1492, 10.1029/2012jd018291, 2013.

1163 Wang, X., Pu, W., Ren, Y., Zhang, X., Zhang, X., Shi, J., Jin, H., Dai, M., and Chen, Q.:
1164 Observations and model simulations of snow albedo reduction in seasonal snow
1165 due to insoluble light-absorbing particles during 2014 Chinese survey,
1166 Atmospheric Chemistry and Physics, 17, 2279-2296, 10.5194/acp-17-2279-2017,
1167 2017.

1168 Wang, X., Wei, H., Liu, J., Xu, B., Wang, M., Ji, M., and Jin, H.: Quantifying the light
1169 absorption and source attribution of insoluble light-absorbing particles on Tibetan
1170 Plateau glaciers between 2013 and 2015, The Cryosphere, 13, 309-324,
1171 10.5194/tc-13-309-2019, 2019.

1172 Wei, T., Dong, Z., Kang, S., Qin, X., and Guo, Z.: Geochemical evidence for sources
1173 of surface dust deposited on the Laohugou glacier, Qilian Mountains, Applied
1174 Geochemistry, 79, 1-8, 10.1016/j.apgeochem.2017.01.024, 2017.

1175 Wiscombe, W. J. and Warren, S. G.: A model for the spectral albedo of snow .1. Pure
1176 snow, Journal of the Atmospheric Sciences, 37, 2712-2733,
1177 10.1175/15200469(1980)037<2712:Amftsa>2.0.Co;2, 1980.

1178 Wu, D., Liu, J., Wang, T., Niu, X., Chen, Z., Wang, D., Zhang, X., Ji, M., Wang, X.,
1179 and Pu, W.: Applying a dust index over North China and evaluating the
1180 contribution of potential factors to its distribution, Atmospheric Research, 254,
1181 10.1016/j.atmosres.2021.105515, 2021.

1182 Wu, G., Yao, T., Xu, B., Tian, L., Zhang, C., and Zhang, X.: Dust concentration and
1183 flux in ice cores from the Tibetan Plateau over the past few decades, Tellus B:
1184 Chemical and Physical Meteorology, 62, 10.1111/j.1600-0889.2010.00457.x,
1185 2010.

1186 Xu, J., Kang, S., Hou, S., Zhang, Q., Huang, J., Xiao, C., Ren, J., and Qin, D.:

1187 Characterization of contemporary aeolian dust deposition on mountain glaciers of
1188 western China, *Sci. Cold Arid Reg*, 8, 0009-0021, 2016.

1189 Yang, L., Shi, Z., Xie, X., Li, X., Liu, X., and An, Z.: Seasonal changes in East Asian
1190 monsoon-westerly circulation modulated by the snow-darkening effect of mineral
1191 dust, *Atmospheric Research*, 279, 10.1016/j.atmosres.2022.106383, 2022.

1192 Yao, T., Thompson, L., Yang, W., Yu, W., Gao, Y., Guo, X., Yang, X., Duan, K., Zhao,
1193 H., Xu, B., Pu, J., Lu, A., Xiang, Y., Kattel, D. B., and Joswiak, D.: Different
1194 glacier status with atmospheric circulations in Tibetan Plateau and surroundings,
1195 *Nature Climate Change*, 2, 663-667, 10.1038/nclimate1580, 2012.

1196 Yao, T., Xue, Y., Chen, D., Chen, F., Thompson, L., Cui, P., Koike, T., Lau, W. K. M.,
1197 Lettenmaier, D., Mosbrugger, V., Zhang, R., Xu, B., Dozier, J., Gillespie, T., Gu,
1198 Y., Kang, S., Piao, S., Sugimoto, S., Ueno, K., Wang, L., Wang, W., Zhang, F.,
1199 Sheng, Y., Guo, W., Ailikun, Yang, X., Ma, Y., Shen, S. S. P., Su, Z., Chen, F.,
1200 Liang, S., Liu, Y., Singh, V. P., Yang, K., Yang, D., Zhao, X., Qian, Y., Zhang, Y.,
1201 and Li, Q.: Recent Third Pole's rapid warming accompanies cryospheric melt and
1202 water cycle intensification and interactions between monsoon and environment:
1203 Multidisciplinary approach with observations, modeling, and analysis, *Bulletin of*
1204 *the American Meteorological Society*, 100, 423-444, 10.1175/bams-d-17-0057.1,
1205 2019.

1206 Yuan, T., Chen, S., Huang, J., Wu, D., Lu, H., Zhang, G., Ma, X., Chen, Z., Luo, Y., and
1207 Ma, X.: Influence of dynamic and thermal forcing on the meridional transport of
1208 Taklimakan desert dust in spring and summer, *Journal of Climate*, 32, 749-767,
1209 10.1175/jcli-d-18-0361.1, 2018.

1210 [Zege, E. P., Katsev, I. L., Malinka, A. V., Prikhach, A. S., Heygster, G., and Wiebe, H.:](#)
1211 [Algorithm for retrieval of the effective snow grain size and pollution amount from](#)
1212 [satellite measurements, *Remote Sensing of Environment*, 115, 2674-2685,](#)
1213 [10.1016/j.rse.2011.06.001, 2011.](#)

1214

1215 Zhang, B., Tsunekawa, A., and Tsubo, M.: Contributions of sandy lands and stony
1216 deserts to long-distance dust emission in China and Mongolia during 2000–2006,
1217 *Global and Planetary Change*, 60, 487-504, 10.1016/j.gloplacha.2007.06.001,
1218 2008.

1219 Zhang, X., Li, Z. Q., You, X. N., She, Y. Y., Song, M. Y., and Zhou, X.: Light-Absorbing
1220 Impurities on Urumqi Glacier No.1 in Eastern Tien Shan: Concentrations and
1221 Implications for Radiative Forcing Estimates During the Ablation Period,
1222 *Frontiers in Earth Science*, 9, 2296-6463, 10.3389/feart.2021.524963, 2021.

1223 Zhang, Y., Kang, S., Sprenger, M., Cong, Z., Gao, T., Li, C., Tao, S., Li, X., Zhong, X.,
1224 Xu, M., Meng, W., Neupane, B., Qin, X., and Sillanpää, M.: Black carbon and
1225 mineral dust in snow cover on the Tibetan Plateau, *The Cryosphere*, 12, 413-431,
1226 10.5194/tc-12-413-2018, 2018.

1227 Zhang, Y., Gao, T., Kang, S., Sprenger, M., Tao, S., Du, W., Yang, J., Wang, F., and
1228 Meng, W.: Effects of black carbon and mineral dust on glacial melting on the Muz
1229 Taw glacier, Central Asia, *Science of the Total Environment*, 740, 140056,
1230 10.1016/j.scitotenv.2020.140056, 2020.

1231 Zhang, Y., Gao, T., Kang, S., Shangguan, D., and Luo, X.: Albedo reduction as an
1232 important driver for glacier melting in Tibetan Plateau and its surrounding areas,
1233 Earth-Science Reviews, 220, 10.1016/j.earscirev.2021.103735, 2021.

1234 Zhao, X., Huang, K., Fu, J. S., and Abdullaev, S. F.: Long-range transport of Asian dust
1235 to the Arctic: identification of transport pathways, evolution of aerosol optical
1236 properties, and impact assessment on surface albedo changes, Atmospheric
1237 Chemistry and Physics, 22, 10389-10407, 10.5194/acp-22-10389-2022, 2022.

1238 Zhu, L., Ma, G., Zhang, Y., Wang, J., Tian, W., and Kan, X.: Accelerated decline of
1239 snow cover in China from 1979 to 2018 observed from space, Science of the Total
1240 Environment, 814, 152491, 10.1016/j.scitotenv.2021.152491, 2022.

1241
1242
1243